

# Memory-Enhanced Dynamic Evolutionary Control of Reconfigurable Intelligent Surfaces

F. Zardi,<sup>(1)(2)</sup> G. Oliveri,<sup>(1)(2)</sup> *Senior Member, IEEE*, and A. Massa,<sup>(1)(2)(3)(4)(5)</sup> *Fellow, IEEE*

<sup>(1)</sup> *ELEDIA Research Center (ELEDIA@UniTN - University of Trento)*

DICAM - Department of Civil, Environmental, and Mechanical Engineering

Via Mesiano 77, 38123 Trento - Italy

E-mail: {francesco.zardi, giacomo.oliveri, andrea.massa}@unitn.it

Website: [www.eledia.org/eledia-unitn](http://www.eledia.org/eledia-unitn)

<sup>(2)</sup> *CNIT - "University of Trento" ELEDIA Research Unit*

Via Sommarive 9, 38123 Trento - Italy

Website: [www.eledia.org/eledia-unitn](http://www.eledia.org/eledia-unitn)

<sup>(3)</sup> *ELEDIA Research Center (ELEDIA@UESTC - UESTC)*

School of Electronic Science and Engineering, Chengdu 611731 - China

E-mail: [andrea.massa@uestc.edu.cn](mailto:andrea.massa@uestc.edu.cn)

Website: [www.eledia.org/eledia-uestc](http://www.eledia.org/eledia-uestc)

<sup>(4)</sup> *ELEDIA Research Center (ELEDIA@TSINGHUA - Tsinghua University)*

30 Shuangqing Rd, 100084 Haidian, Beijing - China

E-mail: [andrea.massa@tsinghua.edu.cn](mailto:andrea.massa@tsinghua.edu.cn)

Website: [www.eledia.org/eledia-tsinghua](http://www.eledia.org/eledia-tsinghua)

<sup>(5)</sup> *School of Electrical Engineering*

Tel Aviv University, Tel Aviv 69978 - Israel

E-mail: [andrea.massa@eng.tau.ac.il](mailto:andrea.massa@eng.tau.ac.il)

Website: <https://engineering.tau.ac.il/>

*This work has been submitted to the IEEE for possible publication. Copyright may be transferred without notice, after which this version may no longer be accessible*

# Memory-Enhanced Dynamic Evolutionary Control of Reconfigurable Intelligent Surfaces

F. Zardi, G. Oliveri, and A. Massa

## Abstract

An innovative evolutionary method for the dynamic control of reconfigurable intelligent surfaces (*RIS*s) is proposed. It leverages, on the one hand, on the exploration capabilities of evolutionary strategies and their effectiveness in dealing with large-scale discrete optimization problems and, on the other hand, on the implementation of memory-enhanced search mechanisms to exploit the time/space correlation of communication environments. Without modifying the base station (*BS*) beamforming strategy and using an accurate description of the meta-atom response to faithfully account for the micro-scale *EM* interactions, the *RIS* control (*RISC*) algorithm maximizes the worst-case *throughput* across all users without requiring that the Green's partial matrices, from the *BS* to the *RIS* and from the *RIS* to the users, be (separately) known/measured. Representative numerical examples are reported to illustrate the features and to assess the potentialities of the proposed approach for the *RISC*.

**Key words:** Reconfigurable Passive *EM* Skins; Smart Electromagnetic Environment; Next-Generation Communications; Metamaterials; Metasurfaces; Evolutionary Optimization; Genetic Algorithm.

# 1 Introduction and Motivation

The Smart Electromagnetic Environment (*SEME*) paradigm is the core of a revolutionary approach for the implementation, the deployment, and the operation of wireless communication systems of next generations mobile networks [1]-[7]. As a matter of fact, the fundamental concept of a *SEME*, that is the opportunistic exploitation of the environment to improve the quality-of-service (*QoS*) at the users of a wireless network, will require a deep revisitation of current communication systems from both the architectural and the operative viewpoints [1]-[7]. To implement the *SEME* vision, several technologies with different levels of complexity have been proposed including integrated access and back-haul (*IAB*) nodes, smart repeaters (*SRs*), and different classes of electromagnetic skins (*EMSs*) [7]-[10]. Reconfigurable intelligent surfaces (*RISs*) are Reconfigurable Passive *EM* Skins (*RP-EMSs*), featuring an interesting trade-off between power consumption, implementation complexity, fabrication costs, and flexibility/reconfigurability [7][11]. A *RIS* usually consists of a combination of elementary meta-atoms, each one embedding at least one electronically-reconfigurable component (e.g., a diode) that controls its scattering parameters [7][11]. By individually adjusting the state of each meta-atom, the *RIS* modifies its local scattering properties so that the macro-scale reflected field fulfils a desired property (e.g., an anomalous direction of reflection) [7][11]. Accordingly, a *RIS* is a passive reflecting device (i.e., the scattered power is always equal or lower than the incident one) that adaptively tailors the wireless response of the environment [7][11]. Therefore, there has been a considerable interest, from both the academic and the industrial communities, on the design, the implementation, and the validation of *RISs* in wireless communications [2][7][12]-[20]. Despite the successful results, several open challenges still exist from the algorithmic and the technological viewpoints before a widespread deployment of *RISs* in large-scale applications. For instance, one of the most challenging items to be addressed is the definition of a suitable *RIS* control (*RISC*) to be (i) used for dynamically adjusting the meta-atom status to yield the envisioned performance improvements at the network level and (ii) easily integrated into the existing infrastructures in an almost seamless fashion with minimum efforts and costs. It is worthwhile to remember that many interesting *RISC* approaches have been proposed in the literature that consider different performance objectives (e.g., minimum transmitter power

[2][12][16], maximum signal-to-interference-plus noise ratio [ $SINR$ ] [14], maximum sum-rate capacity [18]), and/or different constraints (e.g., per-user  $SINR$  [2], total transmitted power [14], per-user capacity [15]), and/or various optimization techniques (e.g., gradient methods [14][18], convex programming [12], as well as random walk [20]). However, despite intrinsic differences, some common features exist among these methods on both the operation principles and the assumptions including the following ones:

- the modification of the beamforming algorithm of the base station ( $BS$ ) to account for the  $RIS$  presence [2][12]-[20]. This implies the replacement of the beamforming methods implemented in current generation  $BS$ s when adding  $RIS$ s;
- the knowledge of the Green's partial matrices from both the  $BS$  to the  $RIS$  and the  $RIS$  to the user terminals [2][12]-[20]. Obtaining such an information in practical scenarios is quite problematic since, on the one hand, it requires the  $RIS$  to include more advanced receiving/decoding/processing capabilities, on the other hand, it implies the exploitation of complex wireless channel estimation mechanisms with a potentially cumbersome overhead [22];
- the assumption that the  $RIS$  meta-atom enables an ideal control of the phase of the reflected wave over a continuous range, sometimes of its magnitude [2][12]-[17], as well. Nevertheless, standard unit cells permit a limited magnitude adjustment and they generally feature very few bits to simplify the control architecture and to reduce the overall costs [21][11];
- the use of idealized  $EMS$ s (e.g., point-like isotropic scatterers), which take into account neither the actual physics of the device nor the presence of induced surface currents [2][12]-[20], for the validation of the  $RISC$ .

This work is aimed at proposing an innovative complement to the existing  $RISC$  approaches for a more easy and reliable deployment of  $RIS$ s in real scenarios. Therefore, the following guidelines are fulfilled: (i) the  $RISC$  method is suitable for existing wireless networks without requiring any modification to the  $BS$  beamforming algorithm; (ii) only the overall “cascaded”

[22] Green's matrix from the *BS* to the user terminals is available as it usually happens in current multi-input multi-output (*MIMO*) communication systems [22]-[24], while there are no information on the Green's partial matrices from/to the *RIS* (i.e., the *RIS* is "blind" with respect to the environment); (iii) the *RISC* method accounts for the limited reconfigurability of typical cost-effective implementations of the unit cells of the *RIS* [11][21] owing to the quantized phase response. Accordingly, a dynamic discrete optimization is formulated to maximize the minimum throughput across all users (i.e., *max-min* criterion to guarantee an adequate *QoS* to all users) subject to a fixed transmitted power and a noise level. The *Generalized Sheet Transition Condition (GSTC)* approach [25]-[30], whose accuracy/reliability has been already assessed in several *SEME* scenarios [11][8], is used to compute the Green's matrix coefficients. Moreover, no direct line-of-sight (*LOS*) links between the *BS* and the mobile terminals are assumed (Fig. 1) in order to primarily analyze the *RIS* effects on the communication *QoS*, while the zero-forcing (*ZF*) method is adopted at the *BS* [23][24] for the beamforming<sup>(1)</sup>.

Owing to the non-linear and discrete nature of the problem at hand as well as the lack of knowledge on the "partial" Green's matrices, which prevents a separate optimization of the *BS* illumination and the *RIS* configuration, an *Evolutionary Algorithm (EA)* [31]-[33] is chosen as solution tool by also exploiting the repetitiveness of the communication scenario (e.g., the instantaneous locations of the terminals) due to the self-similarity of the user trajectories. This latter feature is of fundamental importance in the *RISC* since it allows a minimization of the communication overhead. In particular, the memory-enhanced *EA (ME-EA)* method, previously proposed for adaptive array control [31][32], is customized here to the *RISC*.

To the best of the authors' knowledge, the main methodological novelties of this work with respect to the state-of-the art literature on the topic include

- the introduction of a dynamic *RISC* strategy that allows a considerable reduction of both the complexity of the deployment of *RIS*s in current wireless network architectures and the communications overhead;
- the adoption of a discrete optimization paradigm that, unlike widely adopted methods

---

<sup>(1)</sup>The *ZF* method [23][24] is very popular and diffused, but the same *RISC* can be adopted regardless of the beamforming method at the *BS*.

[2][12]-[18], accounts for the limitations in the reconfiguration of non-ideal *RIS* meta-atoms;

- the implementation of a memory-enhanced *RISC* method that leverages on the information gathered on the time-evolution of the propagation environment rather than repeatedly re-initializing and optimizing the *RIS* status at each update of the communication scenario.

The outline of the paper is as follows. After the formulation of the *RISC* problem (Sect. 2), the proposed *RISC* method is described in Sect. 3. A set of representative numerical results is then reported to assess its effectiveness and reliability also in a comparative fashion (Sect. 4). Finally, some conclusions and final remarks are drawn in Section 5.

## 2 Problem Formulation

With reference to a *MIMO* scenario in a time-harmonic regime, a *BS* composed by  $M$  single-polarization<sup>(2)</sup> radiators, the  $m$ -th ( $m = 1, \dots, M$ ) being located at  $\mathbf{r}_m = (x_m, y_m, z_m)$ , and operating in the multi-user multi-antenna down-link communication mode<sup>(3)</sup> serves at the  $c$ -th ( $c = 1, \dots, C$ ) time instant  $t^{(c)}$  the  $L$  users in Fig. 1 whose positions are  $\{\mathbf{r}_l^{(c)}; l = 1, \dots, L\}$ . Since no direct wireless link can be established between the *BS* and these  $L$  users because of the presence of buildings (Fig. 1), the communication is then enabled by a *RIS*, which is controlled by the *BS* through a dedicated digital channel (Fig. 1). The *RIS*  $\Xi_{\text{RIS}}$ , which comprises  $P$  meta-atoms, is installed on a supporting wall  $\Xi_{\text{wall}}$  and it is centered in the origin of the local coordinate systems  $(x, y, z) = (0, 0, 0)$ . The system composed by the *RIS* and the surrounding wall (Fig. 1) is illuminated at the  $c$ -th ( $c = 1, \dots, C$ ) time-instant by the *BS* with  $B$  incident fields, the  $b$ -th ( $b = 1, \dots, B$ ) being given by

$$\mathbf{E}_b^{(c)}(\mathbf{r}) = \sum_{m=1}^M \mathcal{G}(\mathbf{r}_m, \mathbf{r}) \alpha_{m,b}^{(c)} \hat{\boldsymbol{\chi}} \quad (1)$$

where  $\mathcal{G}$  is the Fourier transform, at the frequency  $f_0$ , of the time-domain Green's tensor component modeling the electromagnetic propagation between the input port of the  $m$ -th ( $m =$

<sup>(2)</sup>The double-polarization case, which is omitted hereinafter for notation simplicity, can be straightforwardly deduced within the same framework.

<sup>(3)</sup>For symmetry reasons, the up-link is neglected.

1, ..., M) transmitting antenna and the vectorial field in  $\mathbf{r}$  [23][24],  $\hat{\chi}$  is the polarization unit vector of the BS antennas, and  $\alpha_{m,b}^{(c)}$  is the  $m$ -th ( $m = 1, \dots, M$ ) excitation of the BS to afford the  $b$ -th ( $b = 1, \dots, B$ ) beam at the  $c$ -th ( $c = 1, \dots, C$ ) time-instant instant.

The  $b$ -th ( $b = 1, \dots, B$ ) field reflected at  $t^{(c)}$  ( $c = 1, \dots, C$ ) by  $\Xi$  ( $\Xi \triangleq \Xi_{RIS} \cup \Xi_{wall}$ ) in far-field is given by [8][9][11]

$$\mathbf{F}_b^{(c)}(\mathbf{r}) = \frac{jk_0 \exp(-jk_0|\mathbf{r}|)}{4\pi|\mathbf{r}|} \int_{\Xi} \left\{ \mathbf{J}_b^{(c)}(\tilde{\mathbf{r}}) \exp(jk_0\hat{\mathbf{r}} \cdot \tilde{\mathbf{r}}) \right\} d\tilde{\mathbf{r}} \quad (2)$$

where  $\mathbf{J}_b^{(c)}$  is the  $b$ -th ( $b = 1, \dots, B$ ) surface (i.e.,  $\mathbf{r} \in \Xi$ ) equivalent current equal to

$$\mathbf{J}_b^{(c)}(\mathbf{r}) = \hat{\mathbf{r}} \times \left[ \eta_0 \hat{\mathbf{r}} \times \mathbf{J}_{b,e}^{(c)}(\mathbf{r}) + \mathbf{J}_{b,h}^{(c)}(\mathbf{r}) \right], \quad (3)$$

$k_0$  and  $\eta_0$  being the free-space wave-number ( $k_0 \triangleq 2\pi f_0 \sqrt{\varepsilon_0 \mu_0}$ ) and the impedance ( $\eta_0 \triangleq \sqrt{\frac{\mu_0}{\varepsilon_0}}$ ), respectively, while  $\varepsilon_0$  is the free-space permittivity and  $\mu_0$  is the permeability  $\mu_0$ . Moreover,  $\mathbf{J}_{b,o}^{(c)}$  ( $o \in \{e, h\}$ ) is the electric/magnetic term of the current  $\mathbf{J}_b^{(c)}$  induced on the surface  $\Xi$ .

Within the RIS region  $\Xi_{RIS}$ , the current components can be computed with the GSTC approach [8][9][11][26]-[30] as follows

$$\begin{aligned} \mathbf{J}_{b,e}^{(c)}(\mathbf{r}) &= j2\pi f_0 \varepsilon_0 \left[ \overline{\overline{\mathbf{K}}}_e^{(c)}(\mathbf{r}) \cdot \tilde{\mathbf{E}}_b^{(c)}(\mathbf{r}) \right]_{\tau} - \hat{\nu} \times \nabla_{\tau} \left[ \overline{\overline{\mathbf{K}}}_h^{(c)}(\mathbf{r}) \cdot \tilde{\mathbf{H}}_b^{(c)}(\mathbf{r}) \right]_{\nu} \\ \mathbf{J}_{b,h}^{(c)}(\mathbf{r}) &= j2\pi f_0 \mu_0 \left[ \overline{\overline{\mathbf{K}}}_h^{(c)}(\mathbf{r}) \cdot \tilde{\mathbf{H}}_b^{(c)}(\mathbf{r}) \right]_{\tau} + \hat{\nu} \times \nabla_{\tau} \left[ \overline{\overline{\mathbf{K}}}_e^{(c)}(\mathbf{r}) \cdot \tilde{\mathbf{E}}_b^{(c)}(\mathbf{r}) \right]_{\nu} \end{aligned} \quad (4)$$

where  $[\cdot]_{\tau/\nu}$  stands for the tangential/normal component,  $\tilde{\mathbf{E}}_b^{(c)}(\mathbf{r})$  ( $\tilde{\mathbf{H}}_b^{(c)}(\mathbf{r})$ ) is the local surface averaged electric (magnetic) field (i.e.,  $\tilde{\mathbf{E}}_b^{(c)}(\mathbf{r}) = \mathcal{F}_e \left\{ \overline{\overline{\mathbf{K}}}_e^{(c)}(\mathbf{r}); \mathbf{E}_b^{(c)}(\mathbf{r}) \right\}$ ,  $\tilde{\mathbf{H}}_b^{(c)}(\mathbf{r}) = \mathcal{F}_h \left\{ \overline{\overline{\mathbf{K}}}_h^{(c)}(\mathbf{r}); \mathbf{H}_b^{(c)}(\mathbf{r}) \right\}$  [8][9][11]), and  $\hat{\nu}$  is the outward normal to the RIS surface  $\Xi_{RIS}$ . Moreover,  $\overline{\overline{\mathbf{K}}}_e^{(c)}$  ( $\overline{\overline{\mathbf{K}}}_h^{(c)}$ ) is the electric (magnetic) local surface susceptibility tensor that describes the micro-scale electromagnetic response of the RIS.

According to the GSTC approach [8][9][11][26]-[30] and subject to the local periodicity condition [8][11][25], the  $o$ -th ( $o \in \{e, h\}$ ) tensor within the RIS (i.e.,  $\mathbf{r} \in \Xi_{RIS}$ ) can be expressed as

$$\overline{\overline{K}}_o^{(c)}(\mathbf{r}) \triangleq \sum_{p=1}^P \left[ \sum_{d=x,y,z} K_o^d(\underline{g}; s_p^{(c)}) \widehat{\mathbf{d}}\widehat{\mathbf{d}} \right] \Omega_p(\mathbf{r}) \quad (5)$$

where  $\Omega_p$  is the basis function related to the  $p$ -th ( $p = 1, \dots, P$ ) meta-atom that occupies the area  $\Xi_p$  of the *RIS* ( $\Xi_{RIS} = \cup_{p=1}^P \{\Xi_p\}$ ) ( $\Omega_p(\mathbf{r}) = \{1 \text{ if } \mathbf{r} \in \Xi_p; 0 \text{ otherwise}\}$ ),  $\underline{g}$  is the  $U$ -sized vector ( $\underline{g} = \{g^{(u)}; u = 1, \dots, U\}$ ) of the micro-scale geometrical/material descriptors of the unit cell of the *RIS* featuring  $\mathcal{B}$  reconfiguration bits, and  $s_p^{(c)}$  is the micro-scale (discrete) status of the  $p$ -th ( $p = 1, \dots, P$ ) *RIS* atom at the  $c$ -th ( $c = 1, \dots, C$ ) time-instant ( $s_p^{(c)} \in \{1, \dots, 2^{\mathcal{B}}\}$ ).

As for the wall region  $\Xi_{wall}$ , equations (4) still hold true provided that the area  $\Xi_{wall}$  is partitioned in  $Q$  sub-regions (i.e.,  $\Xi_{wall} = \cup_{q=1}^Q \{\Xi_q\}$ ) to compute (5) and the associated electric/magnetic local surface susceptibilities are set to a constant value over time (i.e.,  $\overline{\overline{K}}_e^{(c)} \leftarrow \overline{\overline{K}}_e$ ,  $\overline{\overline{K}}_h^{(c)} \leftarrow \overline{\overline{K}}_h$ ) since the supporting wall properties cannot be re-configured.

According to this formulation (2)-(5), once the meta-atom has been designed [i.e.,  $\underline{g}$  is set in (5)], the  $c$ -th ( $c = 1, \dots, C$ ) far-field pattern  $\mathbf{F}_b^{(c)}$  reflected by the surface  $\Xi$  when illuminated by the  $b$ -th ( $b = 1, \dots, B$ ) *BS* beam can be adaptively controlled by acting on the  $M$  *BS* excitations affording the  $b$ -th ( $b = 1, \dots, B$ ) beam,  $\underline{\alpha}_b^{(c)} = \{\alpha_{m,b}^{(c)}; m = 1, \dots, M\}$  and/or the status of the  $P$  meta-atoms of the *RIS*,  $\underline{s}^{(c)} \triangleq \{s_p^{(c)}; p = 1, \dots, P\}$ .

Under the assumptions of [23][24] (i) single-carrier band-pass digitally-modulated signals at the transmitters observed for the duration of a single pulse, (ii) equal power distribution among the down-link beams, (iii) mutual incoherence among the signal and the noise for each beam, (iv) ideal isotropic antenna in reception, the *MIMO* down-link throughput at the  $l$ -th ( $l = 1, \dots, L$ ) receiver in the  $c$ -th ( $c = 1, \dots, C$ ) time-instant,  $\mathcal{T}_l^{(c)}$ , is given by [23][24]

$$\mathcal{T}_l^{(c)} = \log_2 \left( 1 + \frac{|\mathbf{F}_b^{(c)}(\mathbf{r}_l^{(c)})|^2}{\sum_{b=1, b \neq l}^B |\mathbf{F}_b^{(c)}(\mathbf{r}_l^{(c)})|^2 + \frac{L\sigma^2}{\Lambda}} \right) \quad (6)$$

where  $\Lambda$  is the total power radiated by the *BS* and  $\sigma^2$  is the noise power at  $f_0$ , which is assumed to be constant across all the  $L$  receivers for the sake of simplicity.

For a fixed meta-atom geometry,  $\underline{g}$ , the maximization of the minimum *QoS* across all  $L$  users corresponds to the minimization of the *QoS* cost function  $\Phi$  defined as

$$\Phi(\underline{s}^{(c)}, A^{(c)}) = \frac{1}{\mathcal{T}_{\text{worst}}^{(c)}} \quad (7)$$



where  $\mathcal{T}_{\text{worst}}^{(c)} \triangleq \min_{l=1, \dots, L} [\mathcal{T}_l^{(c)}]$ .

Such a cost function (7) depends on the  $c$ -th ( $c = 1, \dots, C$ ) set of the  $B$  beamforming excitations of the  $BS$ ,  $A^{(c)} \triangleq \{\alpha_b^{(c)}; b = 1, \dots, B\}$ , and on the  $c$ -th ( $c = 1, \dots, C$ )  $RIS$  configuration,  $\underline{s}^{(c)}$ . However, to follow the guidelines stated in Sect. 1, the  $ZF$  beamforming method is assumed at the  $BS$  [23][24] so that the resulting  $RISC$  algorithm can blend into existing wireless networks without modifying the  $BS$  operation. More specifically, the optimal beamforming coefficients,  $A_{ZF}^{(c)}$ , are obtained [23][24] as the pseudo-inverse of the discretized version of the overall ‘‘cascaded’’ [22] Green’s matrix from the  $BS$  to the user terminals

$$\Upsilon^{(c)} \triangleq \left\{ v_{l,m}^{(c)}; m = 1, \dots, M; l = 1, \dots, L \right\}, \quad (8)$$

whose  $(l, m)$ -th entry is given by

$$v_{l,m}^{(c)} = \mathbf{F}_b^{(c)} \left( \mathbf{r}_l^{(c)} \right) \Big|_{\mathbf{E}_b^{(c)}(\mathbf{r}_1^{(c)}) = \mathcal{G}(\mathbf{r}_m, \mathbf{r}_l^{(c)}) \alpha_{m,b}^{(c)} \hat{\mathbf{x}}}. \quad (9)$$

As for the computation of  $A_{ZF}^{(c)}$ , it only requires the measurement of  $\Upsilon^{(c)}$  from the  $BS$

$$A_{ZF}^{(c)} \triangleq [\Upsilon^{(c)}]^\dagger, \quad (10)$$

$[\cdot]^\dagger$  being the Moore-Penrose pseudo-inverse operator. It is worth pointing out that, even though  $\Upsilon^{(c)}$  depends on the  $c$ -th ( $c = 1, \dots, C$ )  $RIS$  status,  $\underline{s}^{(c)}$ , according to (9), no cooperation or sensing from the  $RIS$  is needed to implement the proposed  $RISC$  scheme.

Taking into account all previous considerations, the  $RISC$  problem at hand can be finally reformulated into the following dynamic optimization one

*Dynamic RISC Problem* - At each  $c$ -th ( $c = 1, \dots, C$ ) time-instant, given  $g$  and  $A_{ZF}^{(c)}$ ,

find  $\underline{s}_{opt}^{(c)}$  such that

$$\Phi \left( \underline{s}^{(c)} \right) = \Phi \left( \underline{s}^{(c)}, A^{(c)} \right) \Big|_{A^{(c)} = A_{ZF}^{(c)}} \quad (11)$$

is minimized (i.e.,  $\underline{s}_{opt}^{(c)} = \arg [\min_{\underline{s}^{(c)}} \Phi \left( \underline{s}^{(c)} \right)]$ ).

In this problem, the solution space is discrete and the number of solutions  $\mathbb{D}$  grows exponentially

with both the number of *RIS* atoms,  $P$ , and the number of bits-per-atom,  $\mathcal{B}$  ( $\mathbb{D} = 2^{\mathcal{B} \times P}$ ).

### 3 Memory-Enhanced *RIS* Control Algorithm

In principle, the solution of the dynamic *RISC* problem (Sect. 2) may be carried out independently for every  $c$ -th ( $c = 1, \dots, C$ ) time-instant and one instant at a time, but it would neglect the exploitation of the spatial coherence of the time-evolution of the terminal positions and of the resulting  $\Upsilon^{(c)}$  due to the finite speed of any user. Moreover, the typical movement of both pedestrians and vehicles follow repeated “patterns” especially in urban indoor and outdoor scenarios [34]-[39]. Such observations suggest that the *RISC* methods that exploit the correlation between different scenarios could more efficiently identify the optimal *RIS* configuration. Furthermore, the implementation of our *RISC* method must account for (i) the non-linearity of the cost function (11), (ii) the discrete nature of the solution descriptors,  $\underline{s}^{(c)}$ , and (iii) the size of the solution space,  $\mathbb{D}$ . A natural choice to address these challenges is that of recurring to memory-enhanced (*ME*) evolutionary techniques based on Genetic paradigms [31][32]. As a matter of fact,

- such class of methods has been successfully adopted for the control of complex *EM* devices operating in dynamic environments such as phased arrays [31][32];
- the multi-minima and discrete nature of the optimization problem at hand is known to be effectively tackled by Genetic-inspired methodologies [40];
- the underlying paradigm can be customized to account for arbitrary additional constraints and goals without requiring disruptive methodological modifications [31][32].

Accordingly, a memory-enhanced dynamic evolutionary *RISC* method (*ME-RISC*) is proposed in the following according to the flowchart in Fig. 2. Towards this end, the algorithm proposed in [31][32] is extended here to the *Dynamic RISC* problem at hand.

Following the Genetic Algorithm (*GA*) guidelines [40], a multi-step process is performed at each  $c$ -th ( $c = 1, \dots, C$ ) instant,  $t^{(c)}$ , by iteratively applying the Genetic operators to the population of  $\Gamma$  trial solutions  $\mathcal{S}_v^{(c)}$  ( $\mathcal{S}_v^{(c)} = \{\underline{s}^{(c)}|_v^\gamma; \gamma = 1, \dots, \Gamma\}$ ,  $\gamma$  and  $v$  being the solution index and

the iteration index, respectively). At the beginning of the  $c$ -th ( $c = 1, \dots, C$ ) optimization step, an initial population  $\mathcal{S}_0^{(c)}$  is randomly-generated by setting its  $\gamma$ -th ( $\gamma = 1, \dots, \Gamma$ ) individual as follows

$$\underline{s}^{(c)}|_0^\gamma \triangleq \left\{ s_p^{(c)}|_0^\gamma = \text{rnd} [1, 2^B]; p = 1, \dots, P \right\}, \quad (12)$$

then the *ME-GA* loop starts ( $v = 1$ ). Firstly, the *Mutation* and the *Crossover* operators are applied to yield the  $v$ -th population  $\mathcal{S}_v^{(c)}$  [32]. Unlike standard *GAs* and to increase the population diversity, the mutation probability  $\rho_v^{(c)}$  and the crossover probability  $\psi_v^{(c)}$  are dynamically updated in the range  $\rho_v^{(c)} \in [\rho_{\min}, \rho_{\max}]$  and  $\psi_v^{(c)} \in [\psi_{\min}, \psi_{\max}]$ , respectively, by means of the following update rules [32]

$$\begin{aligned} \rho_v^{(c)} &= \rho_{\max} - (\rho_{\max} - \rho_{\min}) \frac{\sigma_v^{(c)}}{\sigma_{\max}} \\ \psi_v^{(c)} &= \psi_{\min} + (\psi_{\max} - \psi_{\min}) \frac{\sigma_v^{(c)}}{\sigma_{\max}} \end{aligned} \quad (13)$$

where  $\sigma_v^{(c)}$  is the variance of the population at the  $v$ -th iteration

$$\sigma_v^{(c)} = \frac{1}{\Gamma} \sum_{\gamma=1}^{\Gamma} \left| \underline{s}^{(c)}|_v^\gamma - \underline{s}_{\text{avg}(v)}^{(c)} \right|^2, \quad (14)$$

$\sigma_{\max}$  being its maximum, while  $\underline{s}_{\text{avg}(v)}^{(c)} = \frac{1}{\Gamma} \sum_{\gamma=1}^{\Gamma} \underline{s}^{(c)}|_v^\gamma$ .

The fitness of all the individuals of the current  $v$ -th population is then evaluated by computing, for each  $\gamma$ -th ( $\gamma = 1, \dots, \Gamma$ ) one, the corresponding cost function value (11) (i.e.,  $\Phi_v^\gamma \triangleq \Phi(\underline{s}^{(c)}|_v^\gamma)$ ) and the  $v$ -th iteration best individual,  $\underline{s}_{\text{best}(v)}^{(c)}$ , along with the associated fitness value,  $\Phi_{\text{best}(v)}^{(c)}$ , are deduced [i.e.,  $\underline{s}_{\text{best}(v)}^{(c)} = \arg[\min_{\gamma=1, \dots, \Gamma; \tilde{v}=1, \dots, v} \{\Phi(\underline{s}^{(c)}|_{\tilde{v}}^\gamma)\}]$  and  $\Phi_{\text{best}(v)}^{(c)} \triangleq \Phi(\underline{s}_{\text{best}(v)}^{(c)})$ ].

To leverage on the memory acquired by the *EA* during operation, a set of non-conventional Genetic operators is then applied. More in detail, firstly a fraction  $\nu_v^{(c)}$  [ $\nu_v^{(c)} = \nu_{\max} \left(1 - \frac{\sigma_v^{(c)}}{\sigma_{\max}}\right)$ ] of the individuals of the population  $\mathcal{S}_v^{(c)}$  with worse fitnesses are replaced with randomly sampled individuals [32] (“*Population Replacement*” step - Fig. 2). Successively, the indicator  $\Theta_v^{(c)}$  is computed

$$\Theta_v^{(c)} = \sum_{\tilde{v}=1}^{\mathcal{W}} \frac{\Phi_{\text{best}(v)}^{(c)} - \Phi_{\text{best}(v-\tilde{v})}^{(c)}}{2^{\tilde{v}}} \quad (15)$$

(“*Effectiveness Self-Evaluation*” step - Fig. 2) to quantify the effectiveness of the optimization at the  $c$ -th time-instant,  $\mathcal{W}$  being a user-defined observation interval. In (15) and unlike [32], the exponentially-decaying weighting  $2^{\tilde{v}}$  is considered to improve the responsiveness of the *RISC* method to changes in the dynamic scenario.

Depending on the value of  $\Theta_v^{(c)}$ , either the “*Memory Learning*” step ( $\Theta_v^{(c)} \geq 0$ ) or the “*Memory Remembering*” step ( $\Theta_v^{(c)} < 0$ ) is performed. In the former case, the best individual at the current  $v$ -th iteration,  $\underline{s}_{best(v)}^{(c)}$ , is stored into a memory pool of good solutions,  $\Psi$  (denoted hereinafter as the “*memory*”), with probability  $\beta_v^{(c)}$  given by

$$\beta_v^{(c)} = \frac{\Theta_v^{(c)}}{\Theta_{max}^{(c)}} \beta_{max}, \quad (16)$$

$\beta_{max}$  being the maximum probability of storing and  $\Theta_{max}^{(c)} = \max_{\tilde{v}=1, \dots, v} [\Theta_{\tilde{v}}^{(c)}]$ . In the second case, the worst individual of the current population  $\mathcal{S}_v^{(c)}$ ,  $\underline{s}_{worst(v)}^{(c)}$  ( $\underline{s}_{worst(v)}^{(c)} \triangleq \arg [\max_{\gamma=1, \dots, \Gamma; \tilde{v}=1, \dots, v} \{\Phi(\underline{s}_{\tilde{v}}^{(c)})^\gamma\}]$ ), is substituted by the best individual of the *memory*  $\Psi$  with a probability  $\kappa_v^{(c)}$  equal to

$$\kappa_v^{(c)} = \frac{\Theta_v^{(c)}}{\Theta_{max}^{(c)}} \kappa_{max}, \quad (17)$$

$\kappa_{max}$  being the maximum probability of re-storing.

If  $v = V$  or a stagnation condition over the sliding window of length  $\mathcal{W}$  is detected (i.e.,  $|\Phi_{best(v)}^{(c)} - \frac{1}{\mathcal{W}} \sum_{\tilde{v}=1}^{\mathcal{W}} \Phi_{best(v-\tilde{v})}^{(c)}| < \delta$ ,  $\delta$  being the stagnation threshold), then the optimization process is stopped and the  $c$ -th *RIS* setup is outputted by setting  $\underline{s}_{opt}^{(c)} = \underline{s}_{best(v)}^{(c)}$ . Otherwise, the iteration index is updated ( $v \leftarrow v + 1$ ) and the *ME-GA* loop is repeated starting from the application of the *Mutation* and *Crossover* operators.

## 4 Numerical Results

To illustrate the performance and to assess the effectiveness/reliability of the proposed *ME-RISC* method, selected numerical results are reported and discussed in the following with comparisons, as well.

The benchmark scenario refers to a *BS* operating at  $f_0 = 3.5$  [GHz] and composed by  $M =$

$30 \times 30$  half-wavelength spaced single-polarization antennas. The *BS* is located 5 [m] above the ground and it illuminates a *RIS* centered at 5 [m] from the ground in a concrete wall of area  $\Xi_{wall} = 6 \times 7$  [m<sup>2</sup>] and thickness 0.2 [m]. The *RIS* features a side of  $\ell_{RIS} \approx 1.93$  [m] and it consists of  $P = 45 \times 45$  reconfigurable meta-atoms ( $P = 2025$ ) whose micro-scale geometrical/material descriptors (i.e.,  $\underline{g}$ ) have been designed by scaling to  $f_0$  the  $\mathcal{B}$ -bit ( $\mathcal{B} = 3$ ) unit cell described in [21]. The wall has been modeled by setting its relative permittivity to  $\varepsilon_{wall} = 5.24$  and the conductivity to 0.123 [S/m] [41]. Moreover, according to the guidelines in [20], the *BS* power and the environment noise level have been set to  $\Lambda = 46$  [dBm] and  $\sigma^2 = -96$  [dBm], respectively. Finally, the setup of the control parameters of the *ME-RISC* has been chosen according to the literature guidelines in [32][40]:  $\sigma_{max} = 1$ ,  $[\rho_{min}, \rho_{max}] = [0.02, 0.06]$ ,  $[\psi_{min}, \psi_{max}] = [0.6, 0.95]$ ,  $\mathcal{W} = 3$ ,  $\nu_{max} = \kappa_{max} = \beta_{max} = 0.2$ ,  $V = 100$ , and  $\Gamma = 100$ .

The first numerical experiment is aimed at illustrating the working of the *ME-RISC* method. Towards this end, the dynamic scenario in Fig. 3 is dealt with where a *BS*, placed at the coordinates  $(x', y', z') = (-20, 20, 5)$  [m] of the global reference system, serves  $L = 3$  users moving for  $C = 100$  subsequent time-instants according to an ‘‘Aperiodic Trajectory’’ in an area of  $\Omega_{user} = 120 \times 80$  [m<sup>2</sup>] in front of the *RIS*. For illustrative purposes, Figure 4(a) gives an idea of the standard behaviour of the *ME-GA* operators during the iterative process at the basis of the *ME-RISC* method. More specifically, the plots of the self-detected efficiency indicator  $\Theta_v^{(c)}$ , the store probability  $\beta_v^{(c)}$ , and the restore probability  $\kappa_v^{(c)}$  during a period of 3 successive time instants are shown. As it can be observed, the sign/value of  $\Theta_v^{(c)}$  forces either the exploitation of the memory of the *ME-RISC* [i.e., the ‘‘Individual Restored’’ event - Fig. 4(a)] or the storage of the current best solution into the memory  $\Psi$  [i.e., the ‘‘Individual Stored’’ event - Fig. 4(a)]. As a result of the memory use, the worst *MIMO* down-link throughput,  $\mathcal{T}_{worst}^{(c)}$ , yielded by the *ME-RISC* turns out to be always (i.e.,  $\forall c \in [1, C]$ ) greater than that when applying a standard *GA* without memory-based operators (‘‘*GA-RISC*’’) (i.e.,  $\mathcal{T}_{worst}^{(c)} \Big|_{ME-RISC} > \mathcal{T}_{worst}^{(c)} \Big|_{GA-RISC}$  - Fig. 4(b)].

The motivation for such a performance improvement can be inferred by the plot of the difference between the optimal configuration of the *RIS* at a  $c$ -th ( $c = 1, \dots, C$ ) time-instant,  $\underline{s}_{opt}^{(c)}$ , and that

at the initial iteration (i.e.,  $v = 1$ ) of the *ME-GA* algorithm in the same instant,  $\underline{s}_{best(1)}^{(c)}$

$$\Delta \underline{s}^{(c)} = \left| \underline{s}_{best(1)}^{(c)} - \underline{s}_{opt}^{(c)} \right|. \quad (18)$$

By comparing the color-maps of  $\Delta \underline{s}_{ME-RISC}^{(c)}$  [Fig. 5(a)] and  $\Delta \underline{s}_{GA-RISC}^{(c)}$  [Fig. 5(b)] at a representative time-instant (e.g.,  $c = 20$ ), one can deduce that the “memory” mechanism allows an initialization of the *RIS* configuration closer to the optimal one (i.e.,  $\Delta s_p^{(c)} \rightarrow 0, p = 1, \dots, P$ ), hence reducing the optimization burden/time and speeding-up the convergence to the optimal *RIS* setup.

The advantage of deploying a *RIS* controlled by the *ME-RISC* is further highlighted by the plots of the *MIMO* down-link throughput at the  $L$  receiver during the  $C$  time-steps,  $\mathcal{T}_l^{(c)}$  ( $c = 1, \dots, C$ ),  $l = 1, \dots, L$ , shown in Fig. 6. Whatever the  $l$ -th ( $l = 1, \dots, L$ ) the user, the throughput is improved (i.e.,  $\mathcal{T}_l^{(c)} \Big|_{w/RIS} > \mathcal{T}_l^{(c)} \Big|_{w/oRIS}, l = 1, \dots, L$ ) and the control strategy yields a *QoS* fairness among all users (i.e.,  $\mathcal{T}_1^{(c)} \Big|_{w/RIS} \approx \mathcal{T}_l^{(c)} \Big|_{w/RIS} \approx \mathcal{T}_L^{(c)} \Big|_{w/RIS}$ ).

For completeness, Figure 7 gives the power footprint  $\mathcal{P}$  (i.e.,  $\mathcal{P}_b^{(c)}(x', y') \triangleq \left| \mathbf{F}_b^{(c)}(\mathbf{r}) \right|_{z'=0}^2$ ,  $\mathbf{r} \in \Omega_{user}$ ) at the  $c$ -th ( $c = 20$ ) instant when the *BS* operates in the scenario without the *RIS* [Fig. 7(a), Fig. 7(c), and Fig. 7(e)] or with the *RIS* [Fig. 7(b), Fig. 7(d), and Fig. 7(f)] and it serves the user  $l = 1$  [Figs. 7(a)-7(b)], the user  $l = 2$  [Figs. 7(c)-7(d)], and the user  $l = L = 3$  [Figs. 7(e)-7(f)]. As expected, adding the *ME-RISC*-controlled *RIS* better focus the power transmitted by the *BS* towards the user to serve [e.g.,  $\mathcal{P}_l^{(c)}(\mathbf{r}_l^{(c)}) \Big|_{w/RIS} > \mathcal{P}_l^{(c)}(\mathbf{r}_l^{(c)}) \Big|_{w/oRIS}$  - ( $l = 1$ ) Figs. 7(a)-7(b); ( $l = 2$ ) Figs. 7(c)-7(d); and ( $l = L = 3$ ) - Figs. 7(e)-7(f)].

Previous outcomes on the benefit of enriching the propagation environment with a *ME-RISC*-controlled *RIS* are confirmed also when dealing with different noise levels. The time evolution of  $\mathcal{T}_{worst}^{(c)}$  ( $c = 1, \dots, C$ ;  $C = 100$ ) for different noise levels (i.e.,  $\sigma^2 \in \{-96, -76, -56\}$  [dBm]) in Fig. 8(a) shows that there is always a considerable improvement of the worst-case throughput [e.g.,  $\mathcal{T}_{worst}^{(c)} \Big|_{w/oRIS}^{\sigma^2} < \mathcal{T}_{worst}^{(c)} \Big|_{w/RIS}^{\sigma^2}$  and  $\mathcal{T}_{worst}^{(c)} \Big|_{w/oRIS}^{\sigma^2=-96 \text{ dBm}} \approx \mathcal{T}_{worst}^{(c)} \Big|_{w/RIS}^{\sigma^2=-76 \text{ dBm}}$  - Fig. 8(a)] as visually further pointed out by the behavior of the average worst-case throughput  $\mathcal{T}_{worst}^{avg}$  ( $\mathcal{T}_{worst}^{avg} \triangleq \frac{1}{C} \sum_{c=1}^C \mathcal{T}_{worst}^{(c)}$ ) versus the noise level [Fig. 8(b)]. This latter proves the boost of the *MIMO* communication performance in all operative conditions [ $\mathcal{T}_{worst}^{avg} \Big|_{w/RIS} > \mathcal{T}_{worst}^{avg} \Big|_{w/oRIS}$

- Fig. 8(b)].

Besides the contribution of the *RIS* installation, it is worth remarking that the proposed *ME-RISC* also opportunistically leverages on the scattering environment - according to the *SEME* paradigm - to enhance the *QoS*. To assess such a feature, another (even more challenging) scenario is considered where both  $\Xi_{RIS}$  and  $\Xi_{wall}$  have been shifted by 10 [m] along the  $x'$  axis with respect to the setup of the first numerical experiment. Such a choice implies that the specular reflection from the wall is towards one of the users (i.e.,  $l = 2$ ) making more difficult the task of the *RIS* to provide a good customer service (i.e., an acceptable throughput to all  $L$  users).

The plots of  $\mathcal{T}_{worst}^{(c)}$  ( $1 \leq c \leq C$ ;  $C = 100$ ) for the cases “w/*RIS*”, “w/o *RIS*”, and “*RIS-Only*” are shown in Fig. 9(a) to give some useful insights to the readers. While it is confirmed the role of the presence of the *RIS* to improve the *QoS* at the users (i.e.,  $\mathcal{T}_{worst}^{(c)} \Big|_{w/o\ RIS} < \mathcal{T}_{worst}^{(c)} \Big|_{w/\ RIS}$ ,  $\forall c \in [1, C]$ ), these plots assess the effective exploitation of the environment, since  $\mathcal{T}_{worst}^{(c)} \Big|_{w/\ RIS} > \mathcal{T}_{worst}^{(c)} \Big|_{RIS-Only}$  ( $\forall c \in [1, C]$ ), which is also pictorially highlighted by the comparison between the power footprints ( $c = 20$ ) in Figs. 9(c)-9(d).

The last test case does not consider aperiodic users’ trajectories (Fig. 3), but it deals with users moving according to periodic patterns [37] as it generally happens to pedestrians in a urban environment. Accordingly, the users’ trajectories [Fig. 10(b)] collected in the “Old Market Square” of Nottingham (UK) [37] [Fig. 10(a)] have been chosen as a realistic benchmark.

The comparison of the evolution of  $\mathcal{T}_{worst}^{(c)}$  in the temporal slot  $90 \leq c \leq C$  ( $C = 100$ ) when configuring the *RIS* with the “*ME-RISC*” method or the “*GA-RISC*” one indicates once again the better performance of the proposed approach in terms of effectiveness to yield a greater throughput as well as convergence speed of the *ME-GA* optimization loop thanks to a suitable use of the *memory* mechanism [i.e.,  $\mathcal{T}_{worst}^{(c)} \Big|_{ME-RISC} > \mathcal{T}_{worst}^{(c)} \Big|_{GA-RISC}$  - Fig. 10(a)]. Indeed, the repetitiveness of the communication scenario, owing to the periodic coincidence of the locations of the users’ terminals, implies that there is an high probability that, at each  $c$ -th ( $c = 1, \dots, C$ ) variation of the propagation conditions, it exists a  $\Psi$ -stored *RIS* configuration which is “almost optimal” as confirmed by the representative plot of  $\Delta_{ME-RISC}^{(c)}$  ( $c = 99$ ) in Fig. 10(b) [vs.  $\Delta_{GA-RISC}^{(c)}$  - Fig. 10(c)].

For completeness, the complete ( $1 \leq c \leq C$ ) time-evolution of the worst-case throughput  $\mathcal{T}_{worst}^{(c)}$  with and without the *RIS* is reported in Fig. 12.

## 5 Conclusions and Final Remarks

A new *RISC* method, called *ME-RISC*, has been proposed to dynamically configure *RIS*s in *MIMO* communication scenarios by maximizing the worst-case throughput across all users. Without requiring either a knowledge on the links from the *BS* to the *RIS* and from the *RIS* to the user terminals or a modification of the beamforming strategy at the *BS*, the method leverages on the effectiveness and the efficiency of a *ME* evolutionary algorithm to optimize the states of the *RIS* meta-atoms, which are characterized by a finite number of bits and electromagnetically modeled with the *GSTC* approach.

The numerical validation has proved that (i) the *ME-GA* algorithm, at the core of the *ME-RISC* method, outperforms standard *GA*-based optimizations in terms of both achievable *QoS* and convergence speed; (ii) the *ME-RISC* constructively exploits the *RIS* as well as the scattering environment to improve the throughput at the users' terminals by fulfilling the key principle of the *SEME* (i.e., the opportunistic exploitation of the environment); (iii) the *ME-RISC* turns out to be reliable and efficient in dealing with aperiodic as well as repetitive users' behaviors, this latter framework being intrinsically the optimal working condition owing to the memory mechanism.

Future works, beyond the scope of this manuscript, will be aimed at validating the proposed control method when integrated in a urban-scale *EM* scenario where more "smart entities" (i.e., *IAB* nodes, *SRs*, static passive *EMs* [*SP-EMs*], etc ...) [7]-[10] coexist and they need to be suitably planned/deployed for yielding an optimal performance/cost/maintenance trade-off.

## Acknowledgements

This work benefited from the networking activities carried out within the Project "SPEED" (Grant No. 6721001) funded by National Science Foundation of China under the Chang-Jiang Visiting Professorship Program, the Project "ICSC National Centre for HPC, Big Data and



Quantum Computing (CN HPC)" funded by the European Union - NextGenerationEU within the PNRR Program (CUP: E63C22000970007), the project DICAM-EXC (Departments of Excellence 2023-2027, grant L232/2016) funded by the Italian Ministry of Education, Universities and Research (MUR), the Project "Smart ElectroMagnetic Environment in TrentiNo - SEME@TN" funded by the Autonomous Province of Trento (CUP: C63C22000720003), and the Project "AURORA - Smart Materials for Ubiquitous Energy Harvesting, Storage, and Delivery in Next Generation Sustainable Environments" funded by the Italian Ministry for Universities and Research within the PRIN-PNRR 2022 Program. A. Massa wishes to thank E. Vico for her never-ending inspiration, support, guidance, and help.

## References

- [1] A. Massa, A. Benoni, P. Da Ru, S. K. Goudos, B. Li, G. Oliveri, A. Polo, P. Rocca, and M. Salucci, "Designing smart electromagnetic environments for next-generation wireless communications," *Telecom*, vol. 2, no. 2, pp. 213-221, 2021.
- [2] Q. Wu and R. Zhang, "Intelligent reflecting surface enhanced wireless network via joint active and passive beamforming," *IEEE Trans. Wireless Commun.*, vol. 18, no. 11, pp. 5394-5409, Nov. 2019.
- [3] M. Barbuto, Z. Hamzavi-Zarghani, M. Longhi, A. Monti, D. Ramaccia, S. Vellucci, A. Toscano, and F. Bilotti, "Metasurfaces 3.0: a New Paradigm for Enabling Smart Electromagnetic Environments," *IEEE Trans. Antennas Propag.*, vol. 70, no. 10, pp. 8883-8897, Oct. 2022.
- [4] M. Di Renzo, M. Debbah, D.-T. Phan-Huy, A. Zappone, M.-S. Alouini, C. Yuen, V. Sciancalepore, G. C. Alexandropoulos, J. Hoydis, H. Gacanin, J. De Rosny, A. Bounceur, G. Lerosey, and M. Fink, "Smart radio environments empowered by reconfigurable AI metasurfaces: An idea whose time has come," *EURASIP J. Wireless Commun. Netw.*, vol. 129, pp. 1-20, 2019.

- [5] M. Di Renzo, A. Zappone, M. Debbah, M.-S. Alouini, C. Yuen, J. De Rosny, and S. Tretyakov, "Smart radio environments empowered by reconfigurable intelligent surfaces: How it works, state of research, and the road ahead," *IEEE J. Sel. Areas Comm.*, vol. 38, no. 11, pp. 2450-2525, Nov. 2020.
- [6] M. Di Renzo, K. Ntontin, J. Song, F. H. Danufane, X. Qian, F. Lazarakis, J. De Rosny, D.-T. Phan-Huy, O. Simeone, R. Zhang, M. Debbah, G. Lerosey, M. Fink, S. Tretyakov, and S. Shamai, "Reconfigurable intelligent surfaces vs. relaying: Differences, similarities, and performance comparison," *IEEE Open J. Comm. Soc.*, vol. 1, pp. 798-807, 2020.
- [7] F. Yang, D. Erricolo and A. Massa, "Guest Editorial - Smart Electromagnetic Environment," *IEEE Trans. Antennas Propag.*, vol. 70, no. 10, pp. 8687-8690, Oct. 2022.
- [8] G. Oliveri, P. Rocca, M. Salucci, and A. Massa, "Holographic smart EM skins for advanced beam power shaping in next generation wireless environments," *IEEE J. Multiscale Multiphysics Computat. Techn.*, vol. 6, pp. 171-182, Oct. 2021.
- [9] G. Oliveri, F. Zardi, P. Rocca, M. Salucci, and A. Massa, "Building a smart EM environment - AI-Enhanced aperiodic micro-scale design of passive EM skins," *IEEE Trans. Antennas Propag.*, vol. 70, no. 10, pp. 8757-8770, Oct. 2022.
- [10] G. Oliveri, F. Zardi, P. Rocca, M. Salucci and A. Massa, "Constrained design of passive static EM skins," *IEEE Trans. Antennas Propag.*, vol. 71, no. 2, pp. 1528-1538, Feb. 2023.
- [11] G. Oliveri, P. Rocca, M. Salucci, D. Erricolo, and A. Massa, "Multi-scale single-bit RP-EMS synthesis for advanced propagation manipulation through system-by-design," *IEEE Trans. Antennas Propag.*, vol. 70, no. 10, pp. 8809-8824, Oct. 2022.
- [12] R. Li, B. Guo, M. Tao, Y.-F. Liu, and W. Yu, "Joint design of hybrid beamforming and reflection coefficients in RIS-aided mmWave MIMO systems," *IEEE Trans. Commun.*, vol. 70, no. 4, pp. 2404-2416, Apr. 2022.
- [13] P. Wang, J. Fang, X. Yuan, Z. Chen, and H. Li, "Intelligent reflecting surface-assisted millimeter wave communications: joint active and passive precoding design," *IEEE Trans. Veh. Technol.*, vol. 69, no. 12, pp. 14960-14973, Dec. 2020.

- [14] H. Xie, J. Xu, and Y.-F. Liu, "Max-Min fairness in IRS-aided multi-cell MISO systems with joint transmit and reflective beamforming," *IEEE Trans. Wireless Commun.*, vol. 20, no. 2, pp. 1379-1393, Feb. 2021.
- [15] C. Huang, A. Zappone, G. C. Alexandropoulos, M. Debbah, and C. Yuen, "Reconfigurable intelligent surfaces for energy efficiency in wireless communication," *IEEE Trans. Wireless Commun.*, vol. 18, no. 8, pp. 4157-4170, Aug. 2019.
- [16] Q. Wu and R. Zhang, "Joint active and passive beamforming optimization for intelligent reflecting surface assisted SWIPT under QoS constraints," *IEEE J. Sel. Areas. Commun.*, vol. 38, no. 8, pp. 1735-1748, Aug. 2020.
- [17] Q.-U.-A. Nadeem, A. Kammoun, A. Chaaban, M. Debbah, and M.-S. Alouini, "Asymptotic max-min SINR analysis of reconfigurable intelligent surface assisted MISO systems," *IEEE Trans. Wireless Commun.*, vol. 19, no. 12, pp. 7748-7764, Dec. 2020.
- [18] H. Guo, Y.-C. Liang, J. Chen, and E. G. Larsson, "Weighted sum-rate maximization for reconfigurable intelligent surface aided wireless networks," *IEEE Trans. Wireless Commun.*, vol. 19, no. 5, pp. 3064-3076, May 2020.
- [19] C. Feng, W. Shen, J. An, and L. Hanzo, "Joint hybrid and passive RIS-assisted beamforming for mmwave MIMO systems relying on dynamically configured subarrays," *IEEE Internet Things J.*, vol. 9, no. 15, pp. 13913-13926, Aug. 2022.
- [20] H. Zhang, B. Di, Z. Han, H. V. Poor, and L. Song, "Reconfigurable intelligent surface assisted multi-user communications: how many reflective elements do we need?," *IEEE Wireless Commun. Lett.*, vol. 10, no. 5, pp. 1098-1102, May 2021.
- [21] J. C. Liang, Q. Cheng, Y. Gao, C. Xiao, S. Gao, L. Zhang, S. Jin, and T. J. Cui, "An angle-insensitive 3-Bit reconfigurable intelligent surface," *IEEE Trans. Antennas Propag.*, vol. 70, no. 10, pp. 8798-8808, Oct. 2022.
- [22] A. L. Swindlehurst, G. Zhou, R. Liu, C. Pan and M. Li, "Channel estimation with Reconfigurable Intelligent Surfaces - A general framework," *Proc. IEEE*, vol. 110, no. 9, pp. 1312-1338, Sep. 2022.

- [23] G. Oliveri, G. Gottardi, and A. Massa, "A new meta-paradigm for the synthesis of antenna arrays for future wireless communications," *IEEE Trans. Antennas Propag.*, vol. 67, no. 6, pp. 3774-3788, Jun. 2019.
- [24] G. Oliveri, G. Gottardi, N. Anselmi, and A. Massa, "Capacity-driven low-interference fast beam synthesis for next generation base stations," *IEEE Trans. Antennas Propag.*, vol. 70, no. 6, pp. 4472-4484, Jun. 2022.
- [25] F. Yang and Y. Rahmat-Samii, *Surface Electromagnetics with Applications in Antenna, Microwave, and Optical Engineering*, Cambridge, UK: Cambridge University Press, 2019.
- [26] M. A. Ricoy and J. L. Volakis, "Derivation of generalized transition/boundary conditions for planar multiple-layer structures," *Radio Sci.*, vol. 25, pp. 391-405, 1990.
- [27] E. F. Kuester, M. A. Mohamed, M. Piket-May, and C. L. Holloway, "Averaged transition conditions for electromagnetic fields at a metafilm," *IEEE Trans. Antennas Propag.*, vol. 51, no. 10, pt. 1, pp. 2641-2651, Oct. 2003.
- [28] K. Achouri, M. A. Salem, and C. Caloz, "General metasurface synthesis based on susceptibility tensors," *IEEE Trans. Antennas Propag.*, vol. 63, no. 7, pp. 2977-2991, Jul. 2015.
- [29] T. B. A. Senior and J. L. Volakis, *Approximate Boundary Conditions in Electromagnetics*. London, U.K.: Inst. Elect. Eng., 1995.
- [30] T. B. A. Senior and J. L. Volakis, "Sheet simulation of a thin dielectric layer," *Radio Sci.*, vol. 22, pp. 1261-1272, 1987.
- [31] S. Caorsi, M. Donelli, A. Lommi, and A. Massa, "A real-time approach to array control based on a learned genetic algorithm", *Microw. Opt. Technol. Lett.*, vol. 36, no. 4, pp. 235-238, Jan. 2003.
- [32] A. Massa, M. Donelli, F. G. B. De Natale, S. Caorsi, and A. Lommi, "Planar antenna array control with genetic algorithms and adaptive array theory," *IEEE Trans. Antennas Propag.*, vol. 52, no. 11, pp. 2919-2924, Nov. 2004.

- [33] M. Benedetti, R. Azaro, and A. Massa, "Memory enhanced *PSO*-based optimization approach for smart antennas control in complex interference scenarios," *IEEE Trans. Antennas Propag.*, vol. 56, no. 7, pp. 1939-1947, Jul. 2008.
- [34] A. Grigorev, Z. Tian, S. Rho, J. Xiong, S. Liu, and F. Jiang, "Deep person re-identification in UAV images," *EURASIP J. Advances Signal Process.*, vol. 2019, no. 1, Dec. 2019.
- [35] Y. Wu, Y. Lin, X. Dong, Y. Yan, W. Ouyang, and Y. Yang, "Exploit the unknown gradually: one-shot video-based person re-identification by stepwise learning," *2018 IEEE/CVF Conf. Comput. Vision Pattern Recognition*, Salt Lake City, UT, 18-23 June 2018, pp. 5177-5186.
- [36] M. Bonetto, P. Korshunov, G. Ramponi, and T. Ebrahimi, "Privacy in mini-drone based video surveillance," *2015 11th IEEE Int. Conf. Workshops Autom. Face Gesture Recognit.*, Ljubljana, SI, 4-8 May 2015.
- [37] A. Cheshmehzangi and T. Heat, "Urban identities: influences on socio-environmental values and spatial inter-relations," *Procedia - Social Behav. Sci.*, vol. 36, pp. 253-264, 2012.
- [38] S. V. A. Kumar, E. Yaghoubi, A. Das, B. S. Harish, and H. Proenca, "The P-DESTRE: A fully annotated dataset for pedestrian detection, tracking, and short/long-term re-identification from aerial devices," *IEEE Trans. Inf. Forensics Security*, vol. 16, pp. 1696-1708, Nov. 2020.
- [39] S. Zhang, Y. Xie, J. Wan, H. Xia, S. Z. Li, and G. Guo, "WiderPerson: A diverse dataset for dense pedestrian detection in the wild," *IEEE Trans. Multimedia*, vol. 22, no. 2, pp. 380-393, Feb. 2020.
- [40] P. Rocca, M. Benedetti, M. Donelli, D. Franceschini, and A. Massa, "Evolutionary optimization as applied to inverse problems," *Inv. Probl.*, vol. 25, art no. 123003, pp. 1-41, Dec. 2009.
- [41] *Effects of building materials and structures on radiowave propagation above about 100 MHz*, Rec. ITU-R P.2040-2, International Telecommunications Union, Geneva, Switzerland.

land, Sep. 2021. [Online]. Available: [https://www.itu.int/dms\\_pubrec/itu-r/rec/p/R-REC-P.2040-2-202109-1!!PDF-E.pdf](https://www.itu.int/dms_pubrec/itu-r/rec/p/R-REC-P.2040-2-202109-1!!PDF-E.pdf)

## FIGURE CAPTIONS

- **Figure 1.** *Problem geometry* - RIS-enhanced MIMO down-link communication scenario.
- **Figure 2.** *ME-RISC Method (ME-GA Algorithm)* - Flowchart.
- **Figure 3.** *Illustrative Example* (Aperiodic Users' Trajectories;  $\Lambda = 46$  [dBm],  $\sigma^2 = -96$  [dBm]) - Scenario and users' trajectories ( $c = 1, \dots, C$ ;  $C = 100$ ).
- **Figure 4.** *Illustrative Example* (Aperiodic Users' Trajectories;  $\Lambda = 46$  [dBm],  $\sigma^2 = -96$  [dBm]) - Time-evolution of (a) the parameters of the "memory" mechanism and of (b) the worst MIMO down-link throughput  $\mathcal{T}_{worst}^{(c)}$ .
- **Figure 5.** *Illustrative Example* (Aperiodic Users' Trajectories;  $\Lambda = 46$  [dBm],  $\sigma^2 = -96$  [dBm],  $c = 20$ ) - Plot of  $\Delta \underline{s}^{(c)}$  when using (a) the ME-RISC and (b) the GA-RISC for controlling the RIS.
- **Figure 6.** *Illustrative Example* (Aperiodic Users' Trajectories;  $\Lambda = 46$  [dBm],  $\sigma^2 = -96$  [dBm]) - Time-evolution of the the MIMO down-link throughput at the  $l$ -th ( $l = 1, \dots, L$ ) receiver,  $\mathcal{T}_l^{(c)}$  ( $c = 1, \dots, C$ ;  $C = 100$ ) with and without the RIS controlled by the ME-RISC method.
- **Figure 7.** *Illustrative Example* (Aperiodic Users' Trajectories;  $\Lambda = 46$  [dBm],  $\sigma^2 = -96$  [dBm],  $c = 20$ ) - Plot of the footprint pattern  $\mathcal{P}_b^{(c)}(x', y')$  when the BS operates in the scenario (a)(c)(e) without the RIS or (b)(d)(f) with the RIS controlled by the ME-RISC method for serving the user (a)(b)  $l = 1$ , (c)(d)  $l = 2$ , and (e)(f)  $l = L = 3$  ( $b = l$ ).
- **Figure 8.** *Performance Evaluation* (Aperiodic Users' Trajectories;  $\Lambda = 46$  [dBm]) - Plots of (a) the time-evolution ( $c = 1, \dots, C$ ;  $C = 100$ ) of the worst MIMO down-link throughput,  $\mathcal{T}_{worst}^{(c)}$ , in correspondence with different noise levels ( $\sigma^2 \in \{-96, -76, -56\}$  [dBm]) and (b) the behavior of the average worst-case throughput,  $\mathcal{T}_{worst}^{avg}$  versus the noise level  $\sigma^2$ .
- **Figure 9.** *Performance Evaluation* (Aperiodic Users' Trajectories;  $\Lambda = 46$  [dBm],  $\sigma^2 = -96$  [dBm]) - Plots of (a) the time-evolution ( $c = 1, \dots, C$ ;  $C = 100$ ) of the worst

*MIMO* down-link throughput,  $\mathcal{T}_{worst}^{(c)}$ , and (b) the footprint pattern  $\mathcal{P}_b^{(c)}(x', y')$  when the *BS* operates in the scenario (b) without the *RIS* or with the *RIS* controlled by the *ME-RISC* method (c) without or (d) taking into account the environment for serving the user (b)-(d)  $l = 1$  ( $b = l$ ).

- **Figure 10.** *Performance Evaluation* (Periodic Users' Trajectories) - *Old Market Square* in Nottingham (UK): (a) photo and (b) plot of trajectories of pedestrian users [37].
- **Figure 11.** *Performance Evaluation* (Periodic Users' Trajectories;  $\Lambda = 46$  [dBm],  $\sigma^2 = -96$  [dBm]) - Plots of (a) the time-evolution ( $90 \leq c \leq 100$ ) of the worst *MIMO* down-link throughput  $\mathcal{T}_{worst}^{(c)}$  and (b)(c)  $\Delta \underline{s}^{(c)}$  when using (b) the *ME-RISC* or (c) the *GA-RISC* for controlling the *RIS* at the  $c$ -th ( $c = 99$ ) time instant.
- **Figure 12.** *Performance Evaluation* (Periodic Users' Trajectories;  $\Lambda = 46$  [dBm],  $\sigma^2 = -96$  [dBm]) - Time-evolution ( $c = 1, \dots, C$ ;  $C = 100$ ) of the worst *MIMO* down-link throughput,  $\mathcal{T}_{worst}^{(c)}$ .



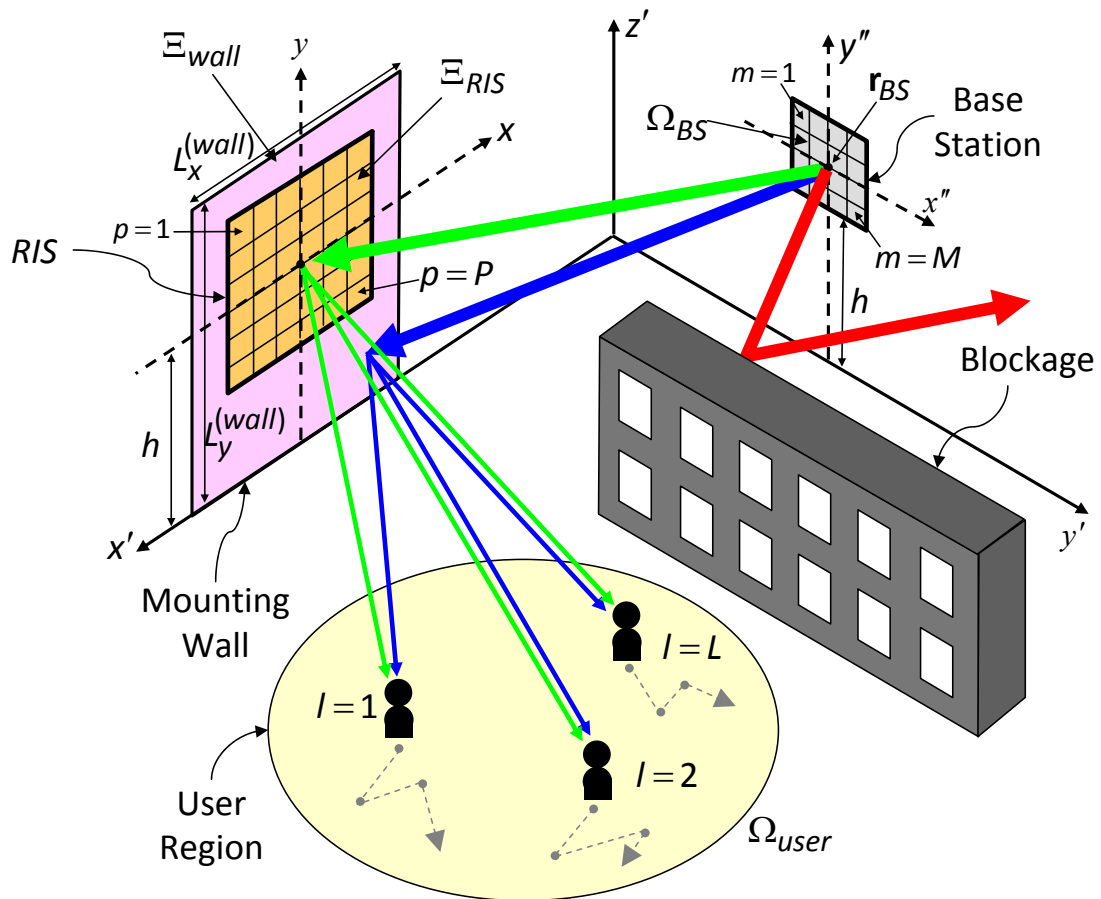


Fig. 1 - F. Zardi et al., "Memory-Enhanced Dynamic Evolutionary Control..."

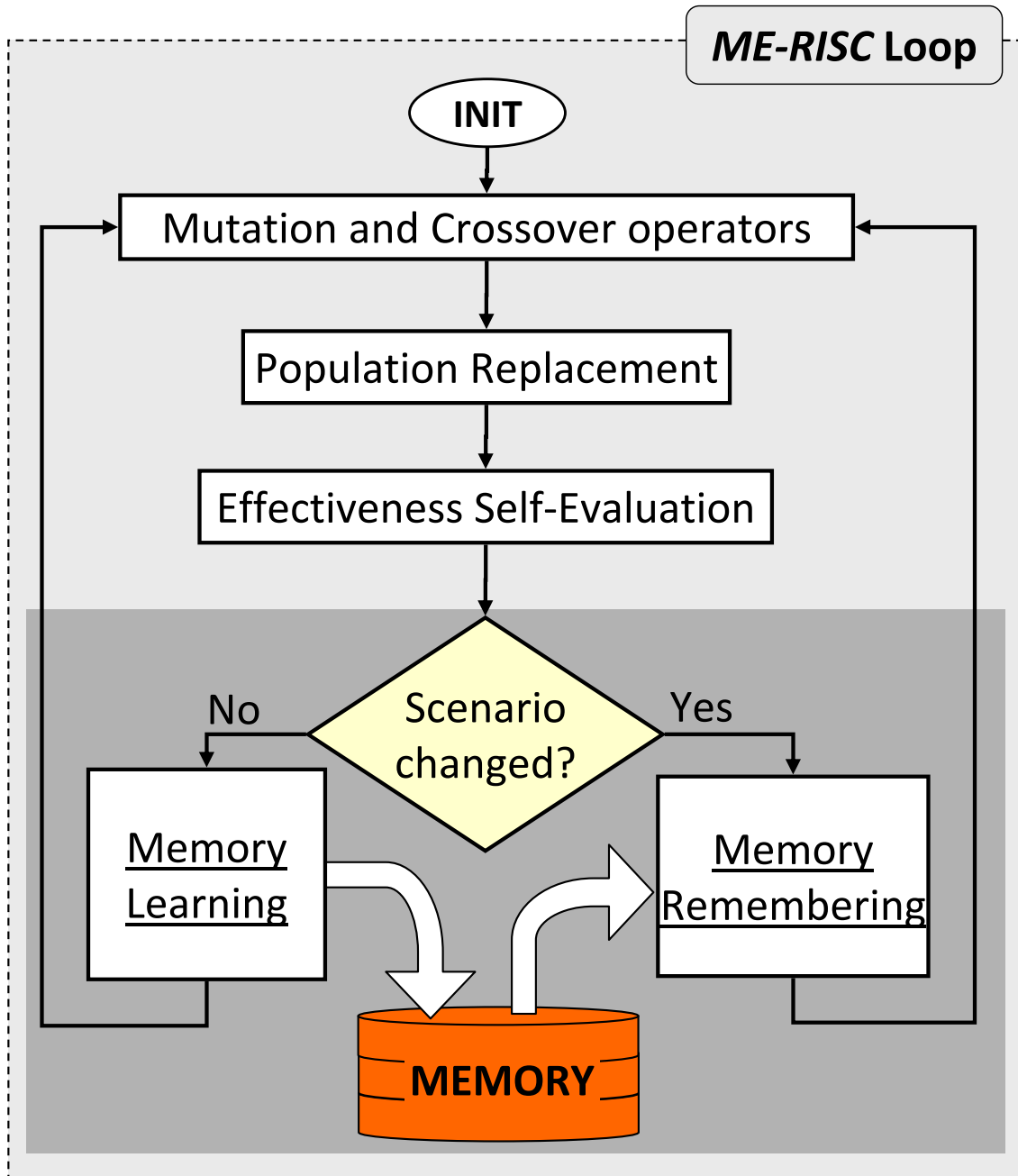


Fig. 2 - F. Zardi et al., “Memory-Enhanced Dynamic Evolutionary Control...”

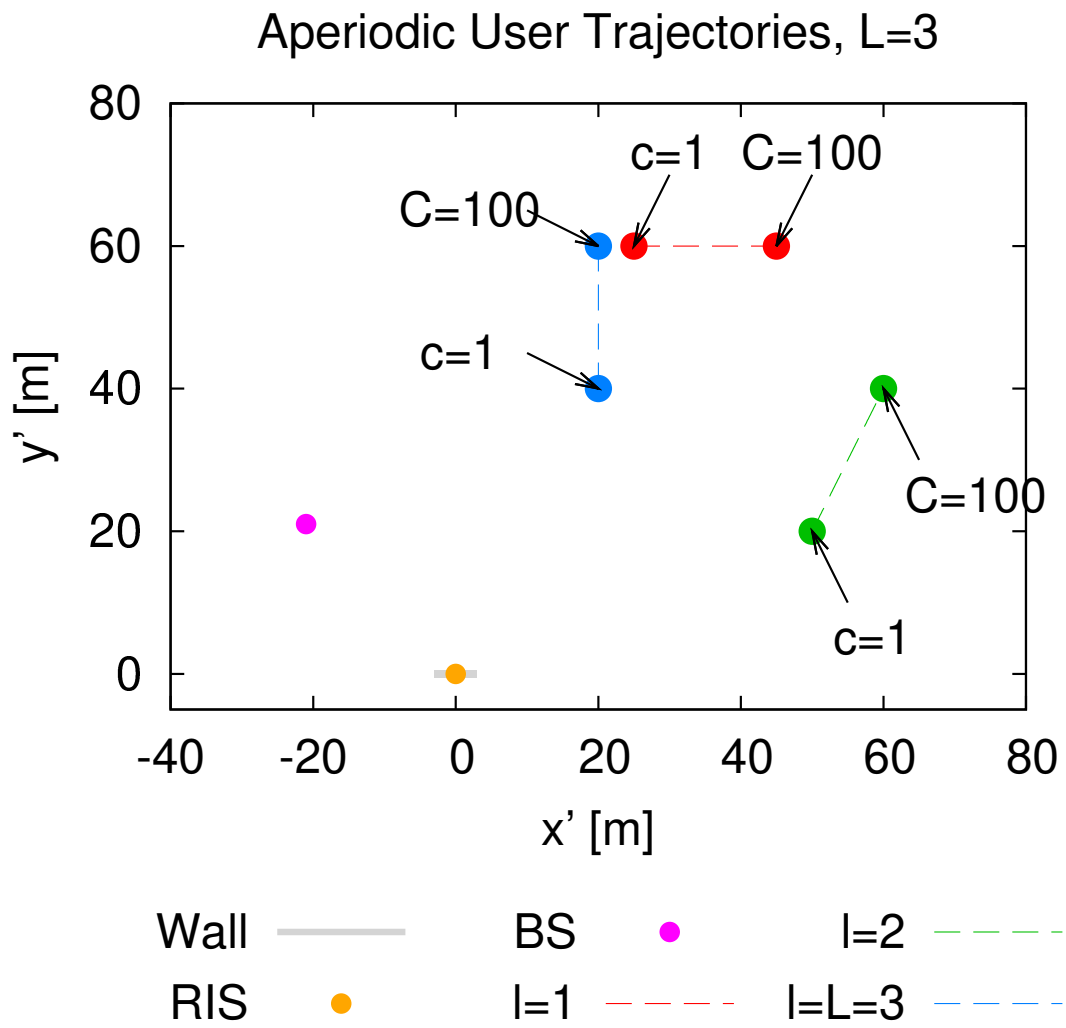
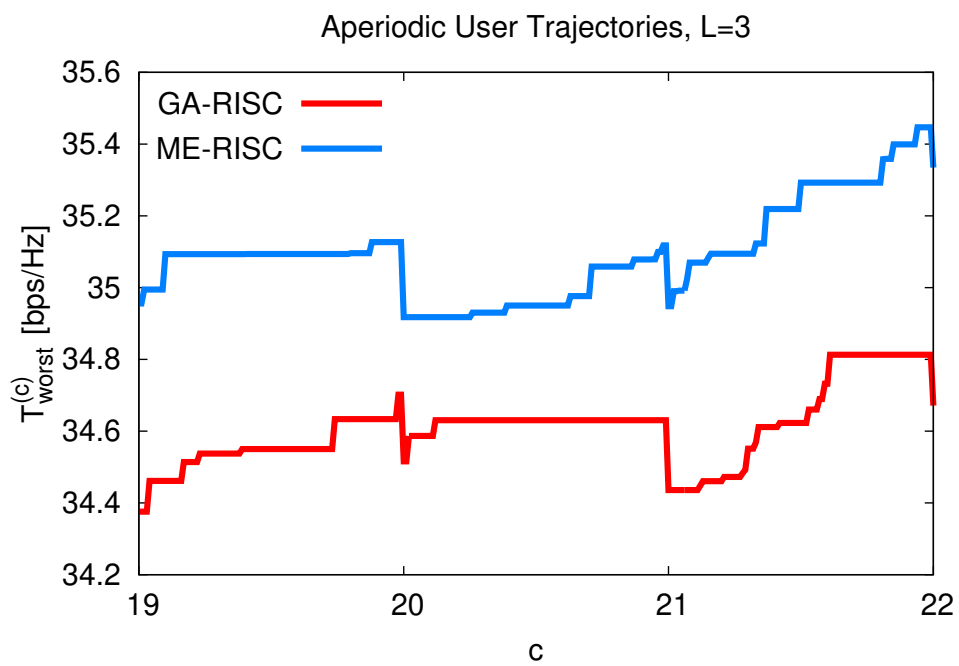
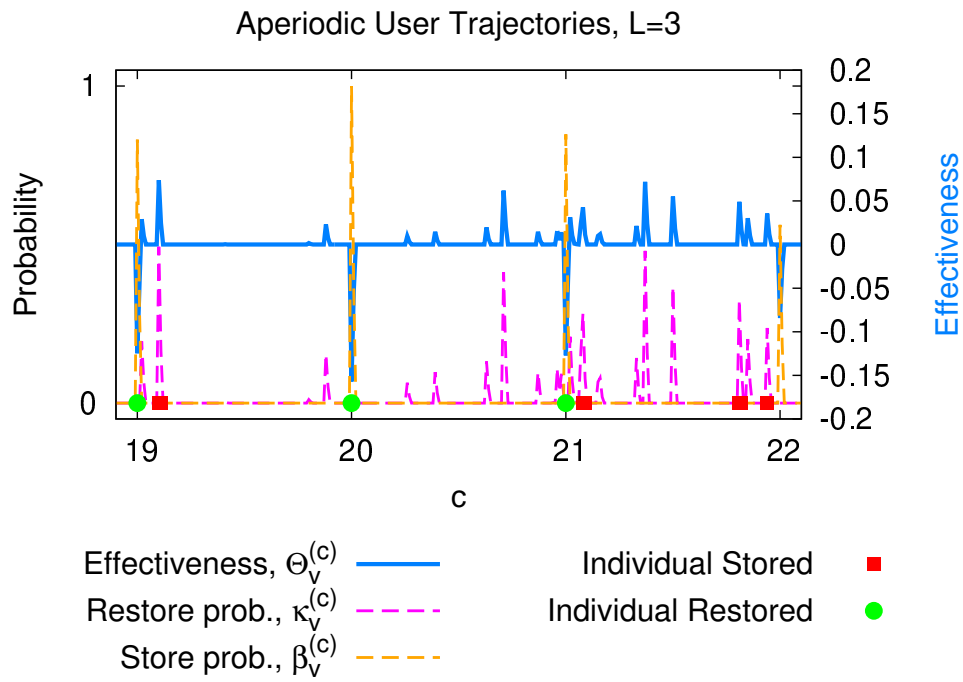
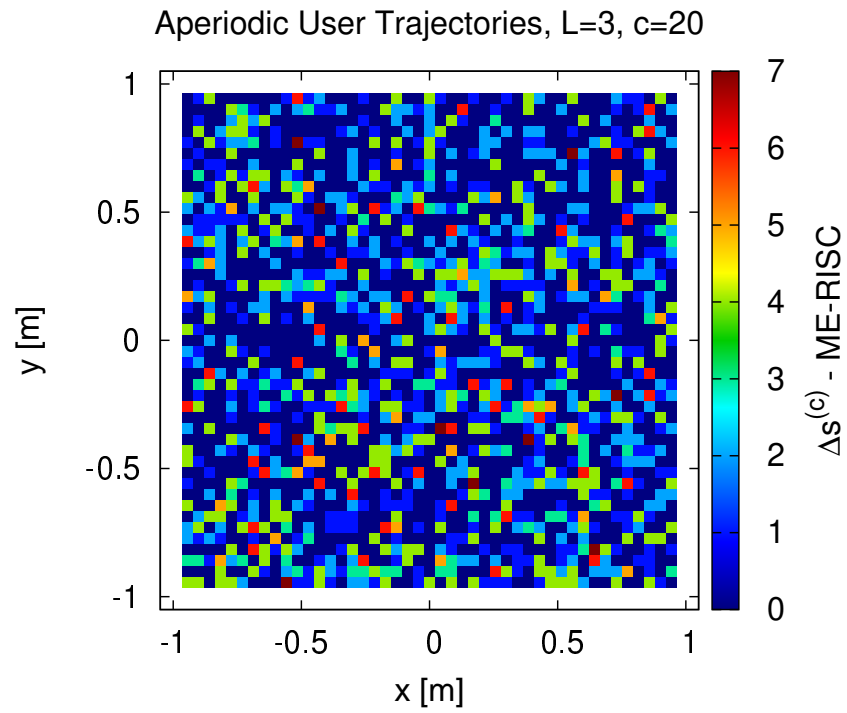


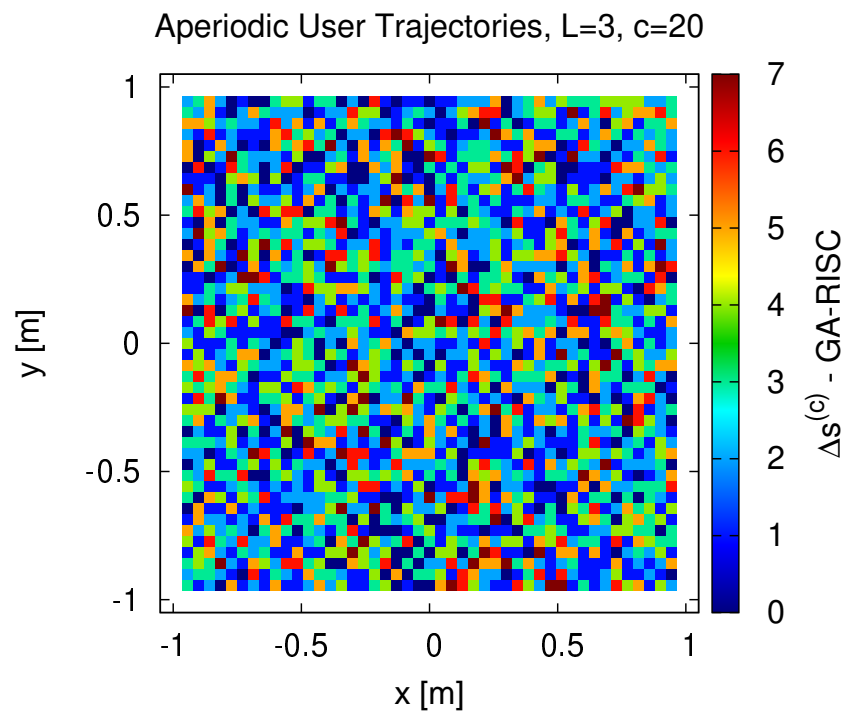
Fig. 3 - F. Zardi et al., "Memory-Enhanced Dynamic Evolutionary Control..."



**Fig. 4 - F. Zardi et al., “Memory-Enhanced Dynamic Evolutionary Control...”**



(a)



(b)

Fig. 5 - F. Zardi et al., “Memory-Enhanced Dynamic Evolutionary Control...”

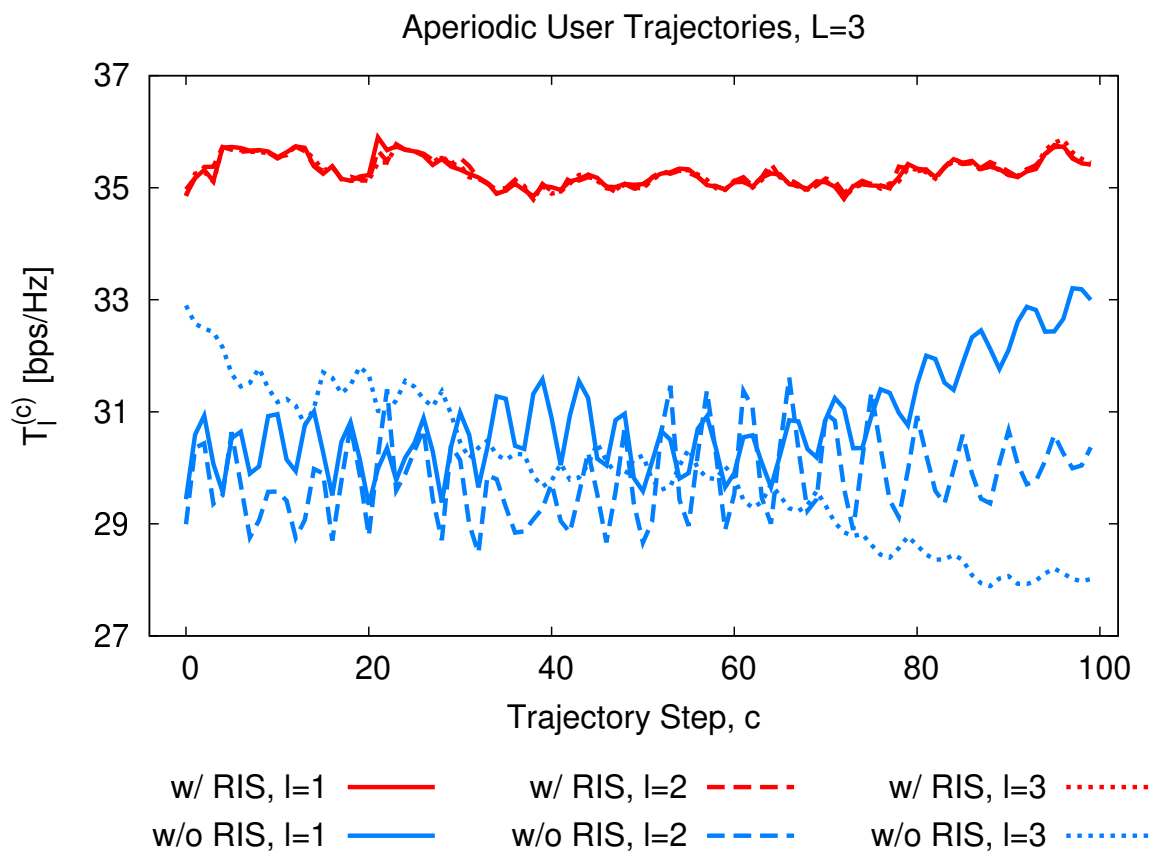


**Fig. 6 - F. Zardi et al., “Memory-Enhanced Dynamic Evolutionary Control...”**

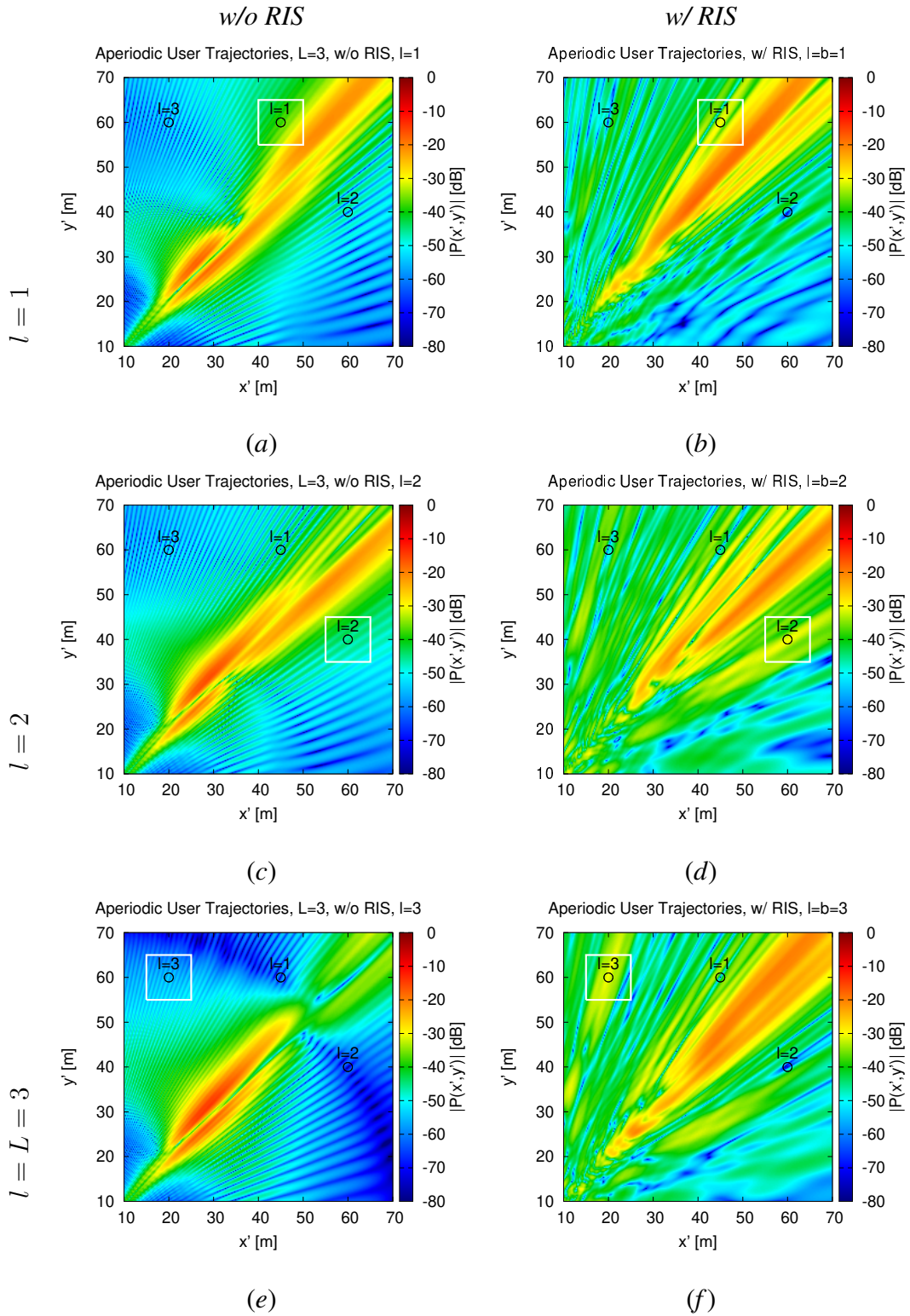


**Fig. 7 - F. Zardi et al., “Memory-Enhanced Dynamic Evolutionary Control...”**

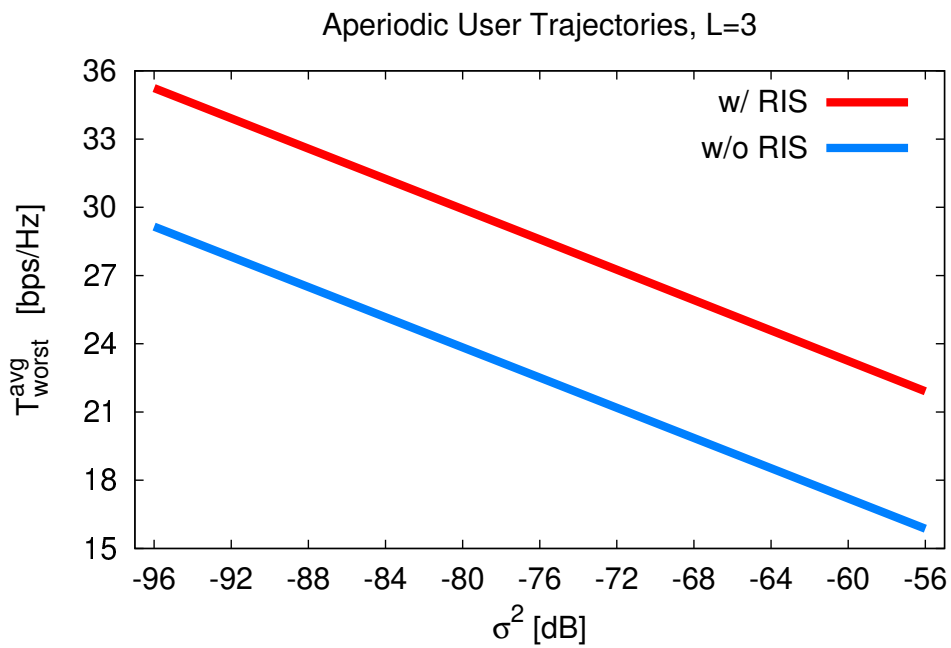
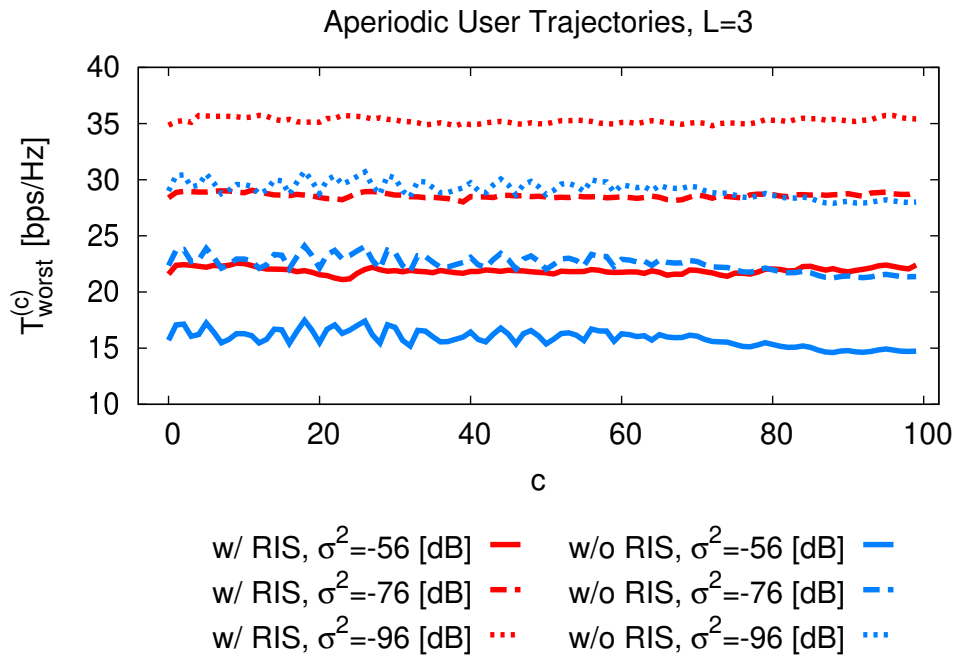
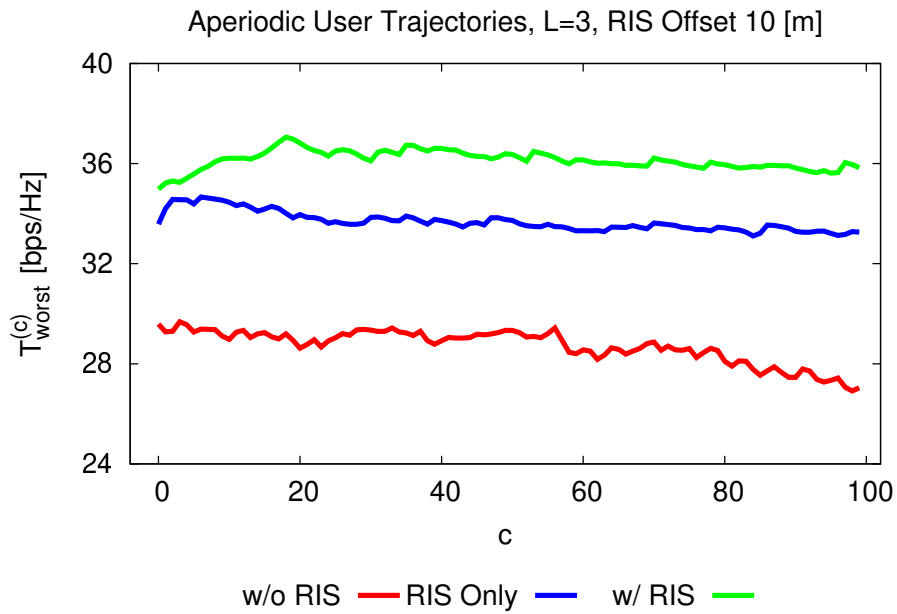
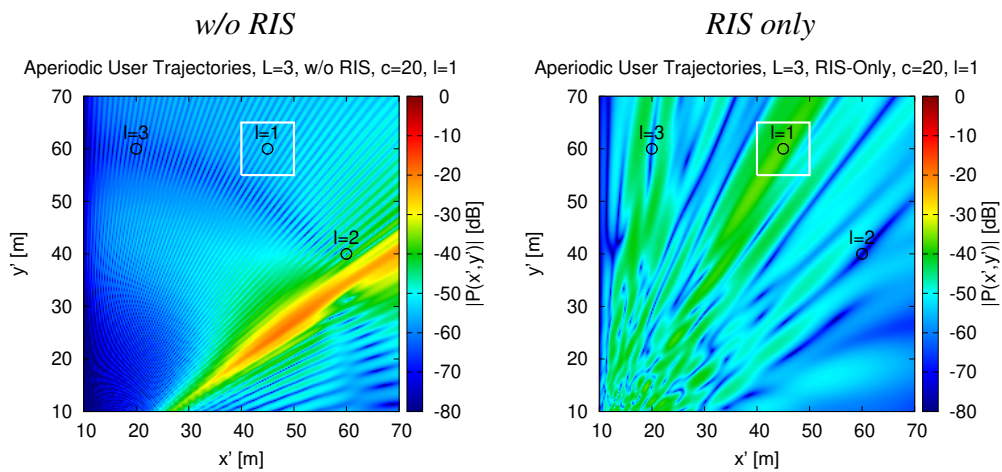


Fig. 8 - F. Zardi et al., "Memory-Enhanced Dynamic Evolutionary Control..."



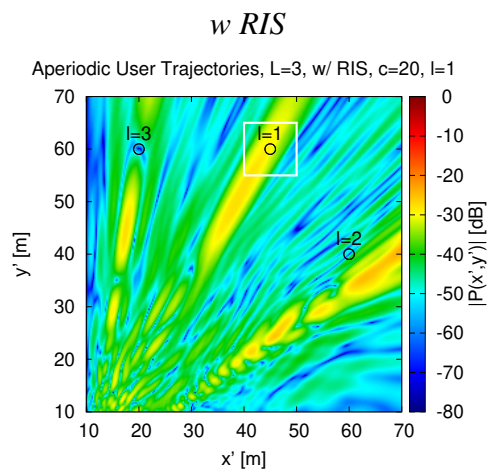


(a)



(b)

(c)



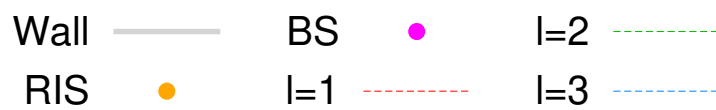
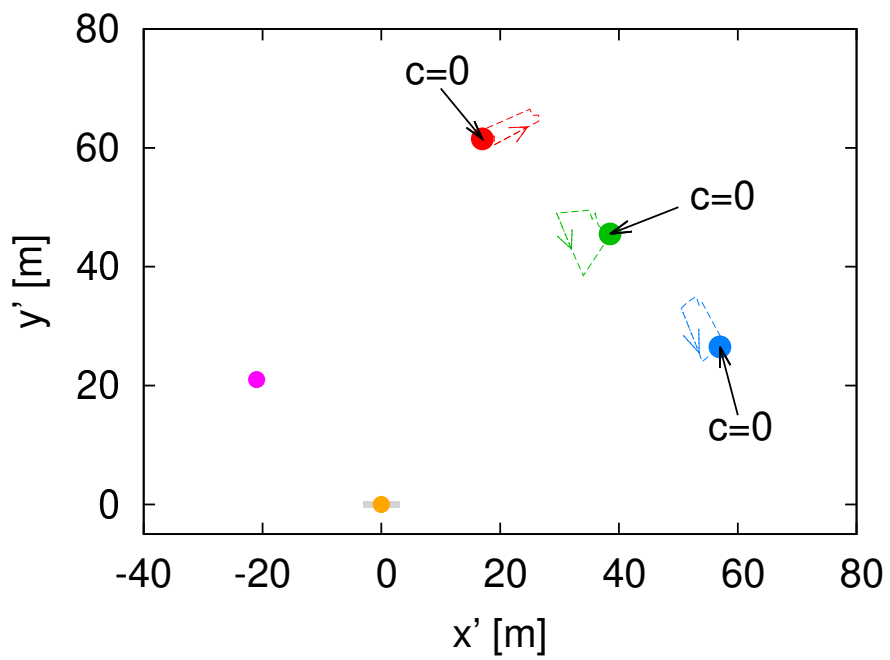
(d)

**Fig. 9 - F. Zardi et al., “Memory-Enhanced Dynamic Evolutionary Control...”**



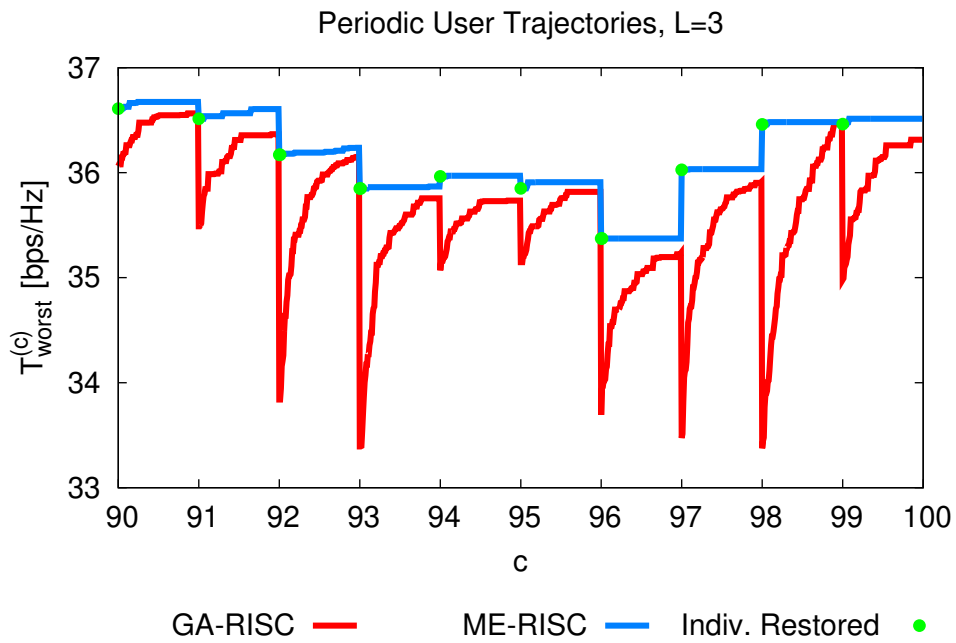
(a)

Periodic User Trajectories,  $L=3$

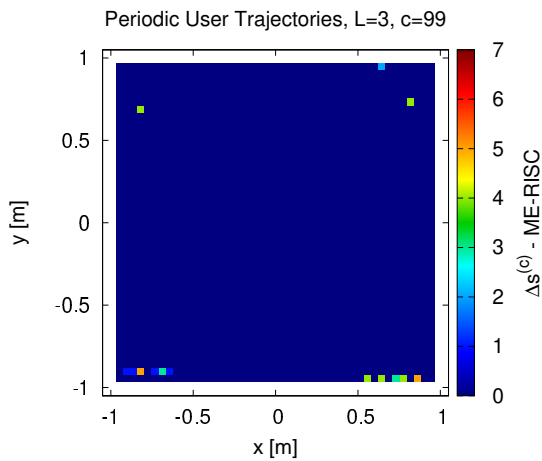


(b)

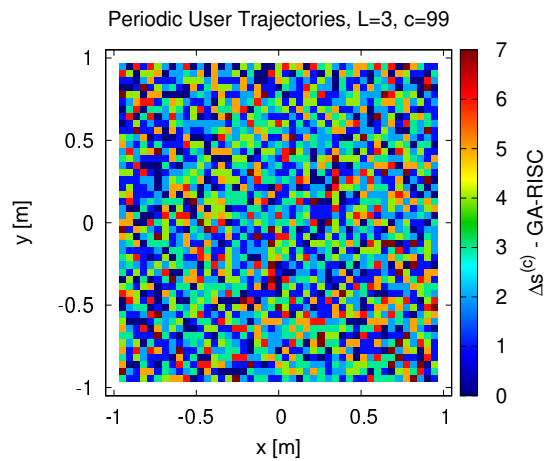
Fig. 10 - F. Zardi et al., “Memory-Enhanced Dynamic Evolutionary Control...”



(a)



(b)



(c)

**Fig. 11 - F. Zardi et al., “Memory-Enhanced Dynamic Evolutionary Control...”**

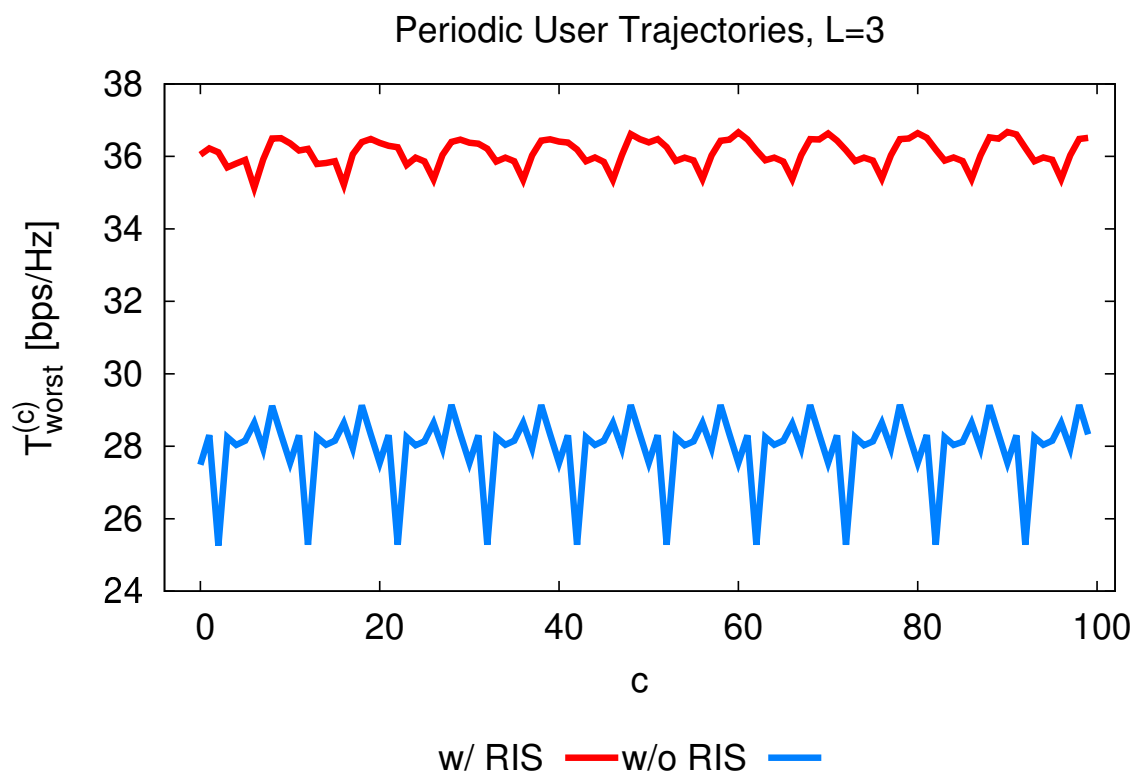


Fig. 12 - F. Zardi et al., “Memory-Enhanced Dynamic Evolutionary Control...”